A numerical investigation of the initiation of aortic dissection

Brian FitzGibbon [a,b], Behrooz Fereidoonnezhad [a], Jamie Concannon [a,b], Niamh Hynes [b], Sherif Sultan [b], Kevin Moerman [a], Patrick McGarry [a,*]

[a] Biomedical Engineering, National University of Ireland Galway, Galway, Ireland
[b] Department of Vascular and Endovascular Surgery, Western Vascular Institute, University College Hospital, Galway, Ireland
*Corresponding author: patrick.mcgarry@nuigalway.ie

Abstract

In the first part of this study we develop a realistic subject-specific aorta finite element model derived from a dual-venc MRI scan. We investigate if spontaneous dissection will occur under extreme hypertensive lumen blood pressure loading, or if significant reduction in interface strength must occur in order for dissection to initiate. Importantly, we also demonstrate that dissection initiation is a pure mode II fracture process, rather than a mixed mode or mode I process. In the second part of this study we construct a parameterised idealised aorta model in order to assess the relative contribution for several anatomical and physiological factors to dissection risk. Such parametric analyses provide fundamental insight into the mechanics of stress localisation and delamination in the aorta. Overall, our detailed series of simulations suggest that variations in anatomical features and hypertensive loading will not result in a sufficient elevation of the stress state in the aorta wall to initiate dissection. Our results suggest that initiation of aortic dissection requires a significant reduction in the mode II fracture strength of the aortic wall, suggesting that dissection is preceded by structural and biomechanical remodelling.

Keywords: *Aortic dissection, aortic arch, finite element, cohesive zone, soft tissue anisotropy*

1 Introduction

Aortic dissection (AD) is a relatively rare but highly lethal disease. Population-based studies indicate incidences of 3.5 aortic dissections per 100,000-person years [1]. One such study reports that 21% of patients died before admission, and, of those hospitalised, 22.7% died within the first 6 hours, 33.3% within the first 12 hours, 50% in the first 24 hours, and 68.2% within 48 hours [2]. Approximately two thirds (62.3%) of cases of AD initiate in the aortic arch, referred to as Stanford type A dissection [3]. Stanford type B dissection refers to dissection initiating distal to the left subclavian artery. AD has been observed spreading to branching vessels in 41% of cases, most frequently to the brachiocephalic and carotid arteries [2].

The underlying mechanics of AD are not well understood. It has been speculated that dissection occurs due to some intimal injury which causes an initial separation of the mural layers of the aorta [4]. Delamination between the elastic lamellae of the media is observed [5]. Propagation of the crack-front is not limited to the circumferential direction; rather, crack spiral-like crack propagation occurs in the circumferential-axial plane, referred to clinically as “spiral barber pole” dissection [6]. Cases in which the crack propagates in the radial direction through the artery wall are nearly always associated with pericardial effusion, leading to cardiac tamponade and death [3,7].

Hypertension is the most common comorbidity associated with AD [3,8]. Chronic hypertension is reported to increase the stiffness of the arterial wall through a pathological process of remodelling [9–12]. A study carried out on pigs with induced hypertension showed that it can lead to the creation of an intra-mural interface where the outer layer of the media becomes hypoxic due to restriction of blood flow to the vasa vasorum [13]. Hypertension also induces hypertrophy of the inner layer of the media [14–16]. Hypertension, therefore, can lead to thickening of the inner layer of the media, arteriosclerosis of the outer layer of the media or of the entire vessel. The effect of such changes on the intramural mechanical stress state has not been previously examined.

During the cardiac cycle the aortic root undergoes significant deformation and displacement [17]. A previous study suggests that forces acting on the aortic root throughout the cardiac cycle may play a role in initiation of AD [18]. The effect of aortic root displacement on wall stress has been preliminarily examined through finite element modelling [19,20]. Such studies consider the circumferential and longitudinal stress in the wall as an indicator of AD potential. However, in the current study we argue that the interface traction along a circumferential-axial plane is a more appropriate metric for examining AD as it pertains to inter-lamellar delamination. The effect anatomical deformation of the aortic root has on interfacial tractions has not yet been examined.

Previous computational studies examining AD have primarily focused on the propagation of an existing dissection or injury rather than the initiation of dissection [21–25]. The authors are not aware of any study presenting a systematic parametric investigation of the individual anatomical and material parameters influencing the initiation of AD. Previous studies predict propagation using mode I fracture strengths calibrated from peel test data [26–29]. In the present study we show that initiation of dissection is a pure mode II process. Furthermore, in our recent experimental study [30] we demonstrate that mode II fracture strength is eight times higher than mode I strength. The authors are not aware of a previous computational analysis of AD in which pure mode II strength and fracture energy are used as model parameters.

In the first part of this study (Section 2) we develop a realistic subject-specific aorta finite element model derived from a dual-venc MRI scan. We investigate if spontaneous dissection will occur under extreme hypertensive lumen blood pressure loading, or if significant reduction in interface strength must occur in order for dissection to initiate. Importantly, we also demonstrate that dissection initiation is a pure mode II fracture process, rather than a mixed mode or mode I process. In the second part of this study (Section 3) we construct a parameterised idealised aorta model in order to assess the relative contribution for several anatomical and physiological factors to dissection risk. Such parametric analyses provide fundamental insight into the mechanics of stress localisation and delamination in the aorta. Overall, our detailed series of simulations suggest that variations in anatomical features and hypertensive loading will not result in a sufficient elevation of the stress state in the aorta wall to initiate dissection. Our results suggest that initiation of AD requires a significant reduction in the mode II fracture strength of the aortic wall, suggesting that dissection is preceded by structural and biomechanical remodelling.

2 Development of a realistic subject-specific model of aortic dissection

2.1 Construction of subject-specific mesh

In the current study we present construction of a subject-specific geometry of the aorta with spatially varying wall thickness. The model includes all major supra-aortic vasculature and major visceral branches. Lumen boundary points and the aortic centreline are extracted directly from MRI data using a bespoke MATLAB framework using the GIBBON toolbox [31,32] (Figure 1(a)). A surface mesh of the main trunk of the aorta is created by sweeping the lumen boundary along the centreline (Figure 1(b)). The major branch vessels of the aorta are added to the surface mesh through a cut and extrusion process (Figure 1(c)). As shown in Figure 1(d), spatially varying wall thickness is accounted for by assigning all vertices with a wall thickness offset, based on reported values in human cadaveric experiments [33]. A structured hexahedral mesh is created by offsetting the surface mesh through the wall thickness (e-f). Each element is assigned a local material orientation (g) and the aorta is modelled as a hyperelastic anisotropic fibre-reinforced material. Unless otherwise stated, the aorta is subject to a hypertensive lumen pressure of 300 mmHg.

Material model

The use of the recently developed constitutive model from Fereidoonnezhad et al. provides improved predictions of aortic anisotropy while facilitating control of unphysical auxetic behaviour [34,35]. The anisotropic strain energy density function due to the presence of two fibre families is given as $\Psi_{aniso} = \sum_{i=1,2} \Psi_{fi}$, where

$$\Psi_{fi} = \begin{cases} E_{1f}\left(\frac{2}{3}\lambda_{fi}^3 - \lambda_{fi}^2 + \frac{1}{3}\right), & \lambda_{fi} - 1 \le D_{1f} \\ \frac{2}{3}\lambda_{fi}^3(q-2p) + \frac{p}{2}\lambda_{fi}^4 + \lambda_{fi}^2(p-q+r) + \psi_{01}, & D_{1f} < \lambda_{fi} - 1 < D_{2f} \\ \frac{2E_{2f}}{3}\lambda_{fi}^3 + \lambda_{fi}^2\left(pD_{2f}^2 + qD_{2f} + r - E_{2f} - E_{2f}D_{2f}\right) + \psi_{02}\,, & \lambda_{fi} - 1 \ge D_{2f} \end{cases} \quad \textbf{(1)}$$

λ_{fi} is the fibre stretch of the i_{th} fibre family, D_{1f} and D_{2f} are material parameters, and p, q and r are given as:

$$p = \frac{E_{1f} - E_{2f}}{2\left(D_{1f} - D_{2f}\right)}, \qquad q = E_{1f} - 2D_{1f}p, \qquad r = \left(E_{1f} - q\right)D_{1f} - pD_{1f}^2, \quad \textbf{(2)}$$

in which E_{1f} and E_{2f} are material parameters. The isochoric strain energy density function is given as

$$\psi_{iso}\left(\bar{\lambda}_1, \bar{\lambda}_2, \bar{\lambda}_3\right) = \sum_{i=1}^{3} \bar{\psi}\left(\bar{\lambda}_i\right),$$

$$\bar{\psi}(\bar{\lambda}_i) = \begin{cases} E_1(\bar{\lambda}_i - \ln\bar{\lambda}_i - 1) & |\bar{\lambda}_i - 1| \le D_1 \\ p\left(\frac{\bar{\lambda}_i^{\,2}}{2} - 2\bar{\lambda}_i + \ln\bar{\lambda}_i\right) + q(\bar{\lambda}_i - \ln\bar{\lambda}_i) + r\ln\bar{\lambda}_i + \psi_{01} & D_1 < |\bar{\lambda}_i - 1| < D_2 \\ E_2(\bar{\lambda}_i - (1+D_2)\ln\bar{\lambda}_i) + (pD_2^2 + qD_2 + r)\ln\bar{\lambda}_i + \psi_{02} & |\bar{\lambda}_i - 1| \ge D_2 \end{cases} \quad (3)$$

where $D_1, D_2, E_1,$ and E_2 are material parameters, $\bar{\lambda}_i$ $(i = 1,2,3)$ are the isochoric principal stretches, $J = \lambda_1\lambda_2\lambda_3$ is the jacobian, and ψ_{01} and ψ_{02} are two constants which ensure the continuity of strain energy. Moreover $p, q,$ and r are not independent parameters; in order to maintain C^0 and C^1 continuity the following relations must be enforced:

$$p = \frac{E_1 - E_2}{2(D_1 - D_2)}, \quad q = E_1 - 2D_1 p, \quad r = (E_1 - q)D_1 - pD_1^2 \quad (4)$$

The ability of the calibrated constitutive law to predict the non-linear anisotropic behaviour of aortic tissue has been previously demonstrated and is shown here in Figure 1(h-i). Slight material compressibility is enforced ($\nu_{eff} = 0.445$) based on the experiments of Nolan et al. [36].

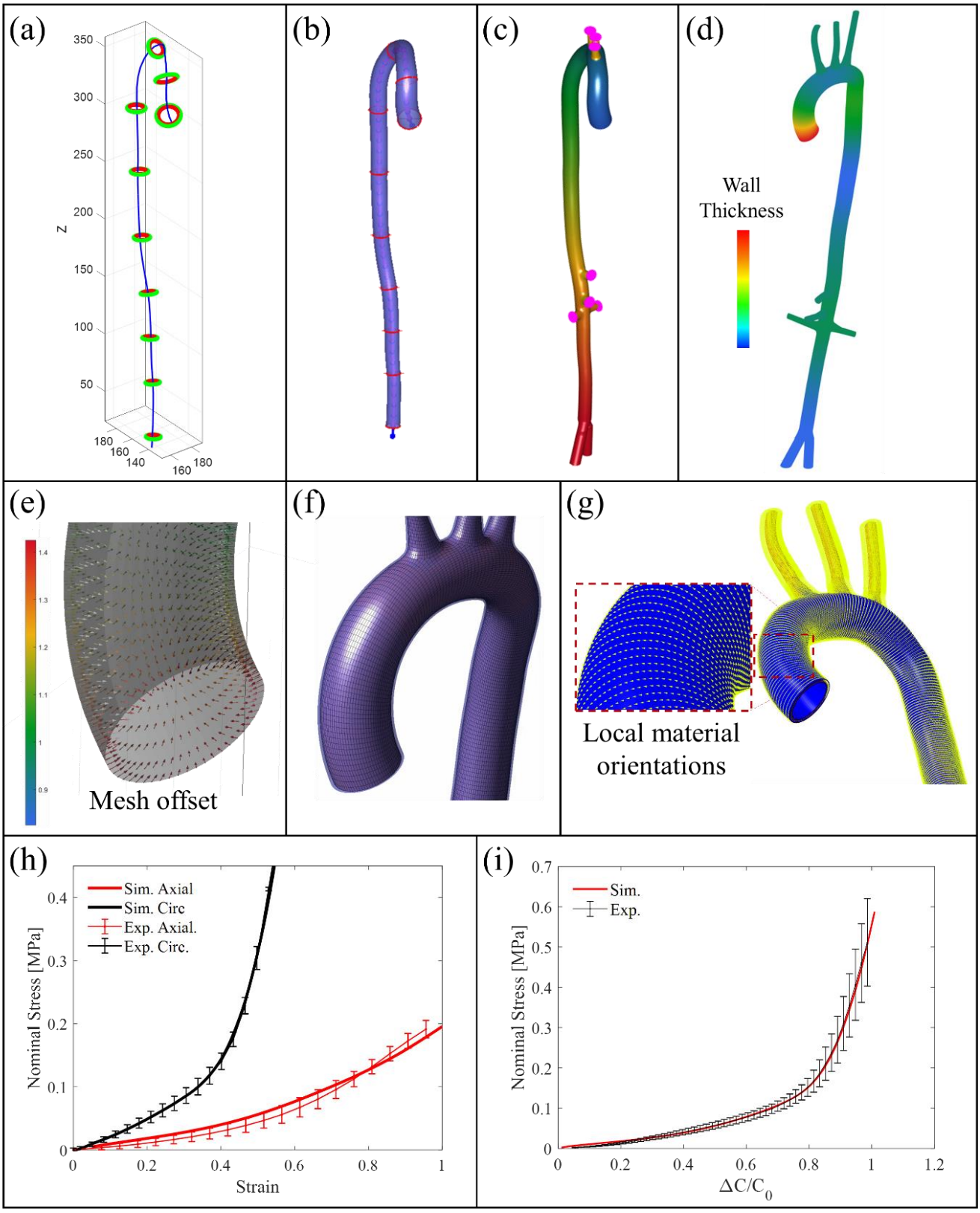

Figure 1. (a-g) Subject-specific aorta mesh creation process (a) Centreline and lumen boundary data extracted from dual-venc MRI; (b) swept surface mesh along the centreline of the main aortic trunk; (c) all major visceral and supra-aortic branch vessels are added to the surface mesh;(d) spatially varying wall thickness assigned to each vertex (e) surface mesh is offset by a spatially varying wall thickness resulting in a structured hexahedral mesh (f); Local material orientations

assigned to each element (local circumferential direction shown in (g)). (h-i) material model calibrated to arterial tissue test data.

Cohesive zone formulation

A cohesive zone formulation [30](Figure 2(a)) is used to describe the mixed-mode traction-separation relationship at the medial interface in the aorta model presented in (shown in Figure 1(f)). For a given interface displacement vector **Δ** with normal and tangential (shear) components Δ_n and Δ_t, respectively, the corresponding displacement magnitude is given as $\Delta_m = \left(\Delta_n{}^2 + \Delta_t{}^2\right)^{1/2}$ and the mode angle is given as $\varphi = \tan^{-1}(\Delta_t/\Delta_n)$. The magnitude of the interface traction is expressed as a function of Δ_m and φ by the following formulation:

$$T_m(\Delta_m, \varphi) = \begin{cases} K_m\Delta_m \,, \Delta_m < \mathrm{T}_m^{max}(\varphi)/K_m \\ K_m\mathrm{T}_m^{max}(\varphi)/K_m\Psi(\varphi) \,, \Delta_m \geq \mathrm{T}_m^{max}(\varphi)/K_m \end{cases} \quad \textbf{(5)}$$

We refer to Ψ as the integrity of the interface (i.e. $\Psi = (1 - D)$, where D is referred to as the interface damage). Ψ monotonically decreases from 1 to 0 with increasing interface separation, such that

$$\Psi(\varphi) = \exp\left(-\frac{\Delta_m^{max} - \mathrm{T}_m^{max}(\varphi)/K_m}{\delta_m^*(\varphi)}\right)\frac{\Delta_m}{\Delta_m^{max}} \quad \textbf{(6)}$$

where K_m is the intrinsic elastic stiffness of the interface. K_m is assumed to be mode-independent. $\mathrm{T}_m^{max}(\varphi)$ is the specified mode-dependent interface strength; the corresponding displacement ($\delta_m^{el}(\varphi) = \mathrm{T}_m^{max}(\varphi)/K_m$) represents the elastic limit of interface separation at the point of damage initiation. The mode-dependent parameter $\delta_m^*(\varphi)$ governs the rate of softening in the damage region ($\Delta_m \geq \mathrm{T}_m^{max}(\varphi)/K_m$). The interface strength is defined as a function of the mode as follows:

$$\mathrm{T}_m^{max}(\varphi) = \tau_{max} - \left(\frac{\tau_{max} - \sigma_{max}}{1 - \exp\left(-\frac{\frac{\pi}{2}}{\Omega^T}\right)}\right)\left(1 - \exp\left(-\frac{\varphi}{\Omega^T}\right)\right) \quad (7)$$

where τ_{max} is the mode II interface strength, Ω^T controls the non-linearity of the transition from mode II to mode I, and σ_{max} is the mode I interface strength. The mode mixity of the initial interface damage parameter $\delta_m^*(\varphi)$ is obtained from

$$\delta_m^*(\varphi) = \frac{G_m(\varphi)}{\mathrm{T}_m^{max}(\varphi)} - \frac{\mathrm{T}_m^{max}(\varphi)}{2K_m} \quad (8)$$

where $G_m(\varphi)$ is the mode-dependent fracture energy

$$G_m(\varphi) = \frac{1}{2}K_m\delta_m^{el}(\varphi)^2 + \int_{\mathrm{T}_m^{max}(\varphi)/K_m}^{\infty} \mathrm{T}_m^{max}(\varphi)\exp\left(-\frac{\Delta_m^{max} - \mathrm{T}_m^{max}(\varphi)/K_m}{\delta_m^*}\right)d\Delta_m \quad \textbf{(9)}$$

We may specify the mode-dependence of $G_m(\varphi)$ using the following function:

$$G_m(\varphi) = G_t^0 - \left(\frac{G_t^0 - G_n^0}{1 - \exp\left(-\frac{\frac{\pi}{2}}{\Omega^G}\right)}\right)\left(1 - \exp\left(-\frac{\varphi}{\Omega^G}\right)\right) \quad \textbf{(10)}$$

where G_t^0 is the mode II fracture energy and G_n^0 is the mode I fracture energy, Ω^G controls the non-linearity of the transition from mode II to mode I (shown in Figure 2(d)). Finally, we complete the description of the cohesive zone formulation by decomposing T_m into the normal and tangential components, T_n and T_t, respectively, such that

$$T_n = \begin{cases} K_{n_{oc}}\Delta_n, \Delta_n < 0 \\ T_m \sin(\varphi), \Delta_n \geq 0 \end{cases} \quad \textbf{(11)}$$

$$T_t = T_m \cos(\varphi) \quad \textbf{(12)}$$

where $K_{n_{oc}}$ is the overclosure penalty stiffness. We include a dependence of the mode II interface strength, τ_{max}, on normal compression at the interface (Figure 2(b)), such that

$$\tau_{max}(T_n) = \begin{cases} \tau_{max}^{nc}(T_n), & \Delta_n < 0 \\ \tau_{max}^0 \quad , & \Delta_n \geq 0 \end{cases}$$

as described in equation **(13)**. The mode II interface strength increases within increasing (negative) normal traction, such that

$$\tau_{max}^{nc}(T_n) = \tau_{max}^0 + \tau_{max}^0(F_{oc} - 1.0) * \left(1 - exp\left(\frac{T_n \frac{K_{n_{oc}}^*}{\sigma_{max}}}{K_m}\right)\right) \quad \textbf{(13)}$$

where $\tau_{max}^{nc}(\Delta_n)$ is the increased value of tangential strength due to a normal compression at the interface. τ_{max}^0 is the maximum tangential strength, as encountered during a pure mode II separation when $\Delta_n = 0$ and $T_n = 0$. The parameter F_{oc} prescribes the maximum (plateau) value of increased shear strength due to compressive normal tractions at the interface. The parameter $K_{n_{oc}}^*$ governs the sensitivity of maximum (plateau) shear stress to compressive normal tractions. However, as a conservative measure, we assume that $\tau_{max} = \tau_{max}^0$, i.e. maximum tangential strength is not increased due to normal compression at the interface in the present study. The normal interface strength calibrated from peel tests is $\sigma_{max} = 202\ kPa$ and the shear interface strength calibrated from shear fracture ring tests is $\tau_{max} = 1.6\ MP$a. Figure 2(c) shows the CZM response under a pure mode I (blue), mode II (red) and mixed mode (black) separation with the aortic tissue fracture properties. This model represents a significant advance over previous models in which the intrinsic elastic stiffness and the fracture energy are coupled [37,38].

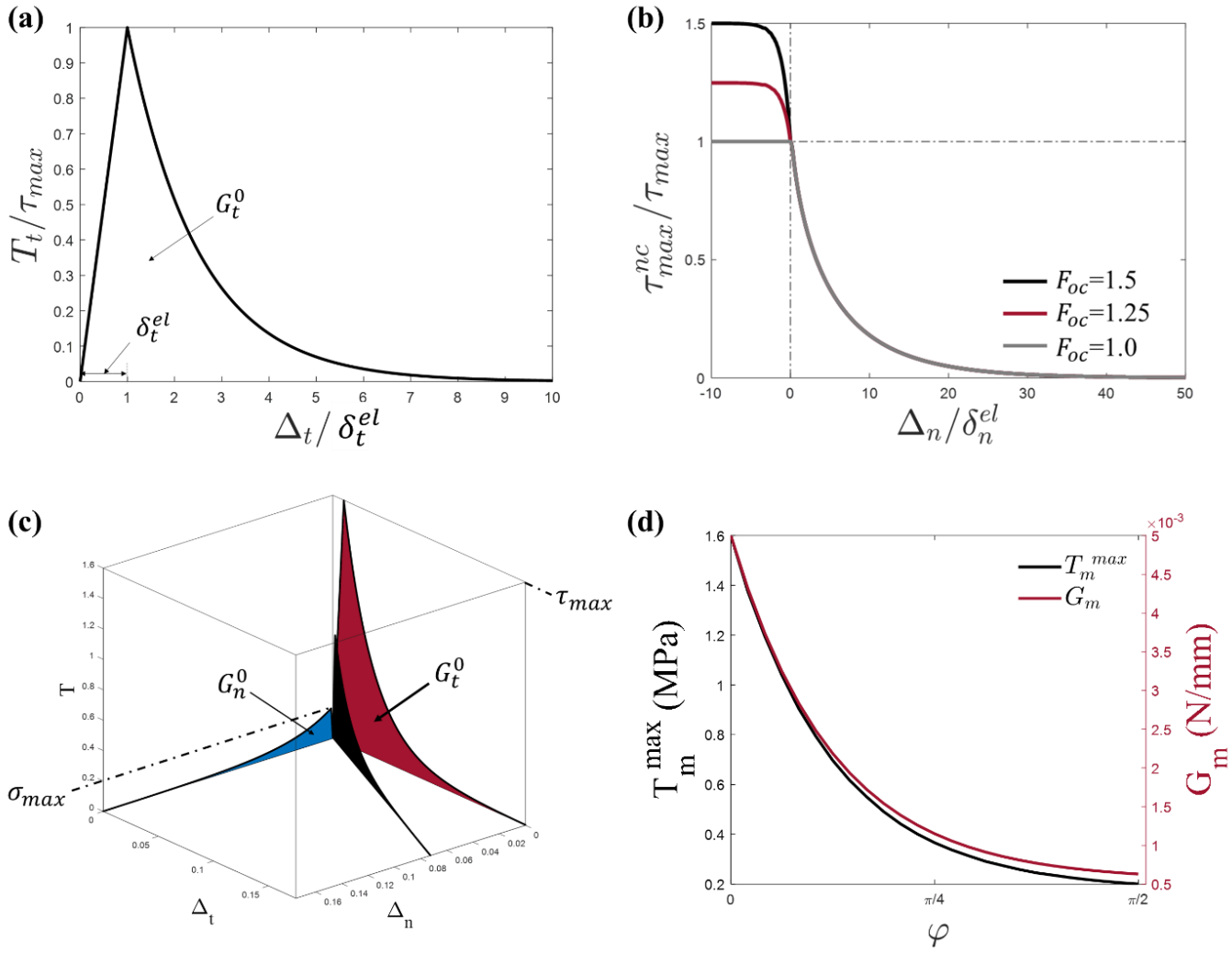

Figure 2. (a) schematic of the cohesive zone model for a pure mode II separation; (b) Augmentation of the mode II interface strength as a function compressive normal traction; (c) CZM traction-separation response to a mode I, mixed mode, and mode II separation with the aortic tissue fracture properties ($\sigma_{max} = 202\ kPa, \tau_{max} = 1.6\ MPa,\ G_t^0 = 0.005\ N/mm, G_n^0 = (\sigma_{max}/\tau_{max})G_t^0$; (d) (left y-axis) interface strength as a function of mode angle φ (right y-axis) fracture energy as a function of mode angle φ.

2.2 Key results for subject-specific aorta model dissection analysis

Figure 3 presents key results computed for the realistic subject-specific aorta model subjected to extreme hypertensive blood pressure loading of 300 mmHg. Figure 3(a) shows that the lumen blood pressure results in a compressive component of local radial stress throughout the aortic wall. This results in negative (compressive) normal tractions along the medial interface (Figure 3(b)). The cohesive zone formulation enforces a strong penalisation of overclosure, such that high negative pressure across the interface results in normal overclosure lower than 5 nanometres (Figure 3(c)). This result indicates that initiation of aortic delamination will be pure mode II, rather than mixed mode or mode I. Informed by this result, we examine the maximum local material shear stress in Figure 3(d). Shear stress concentrations are predicted near the ostia of the supra-aortic branch vessels and along the inner curve of the aortic arch (as shown by the rotated detail view in Figure 3(d)). In order to assess the risk of intramural delamination we examine the shear tractions at the medial interface in Figure 3(e). The predicted shear tractions produce similar trends to the max local material shear stress; high concentrations of shear traction are computed near the ostia of the supra-aortic branch vessels and the inner curve of the aortic arch (Figure 3(e)). Additionally, shear traction concentrations are computed near the ostia of the major visceral branch vessels (contour limits have been adjusted for detailed

inset views to highlight regions of interest). Significant areas of localisation of shear traction are evident at the aortic root, along the arch, and in the descending thoracic aorta. However, all computed maximum shear tractions are approximately two orders of magnitude lower than the experimentally measured mode II fracture strength (τ_{exp}=1.6 MPa), suggesting that even extreme hypertensive loading will not initiate a dissection in healthy aortic tissue. In Figure 3(f) we present results for a series of simulations in which we investigate the influence of a reduced mode II fracture strength on dissection initiation. In the case of hypertensive blood pressure of P=300 mmHg, delamination initiation is not predicted even if the cohesive zone shear strength is reduced to a value of τ_{max}=0.08 Mpa (i.e. 20 times lower than τ_{exp}). If τ_{max} is reduced to a value 100 times lower than τ_{exp} dissection is predicted to initiate at a lumen blood pressure of P=72 mmHg (i.e. approximately at a healthy diastolic blood pressure).

The results presented in Figure 3 indicate that extreme hypertensive lumen blood pressure loading will not result in dissection initiation in healthy aortic tissue (i.e. tissue with a mode II fracture strength of ~1.6 MPa, as measured experimentally), However, chronic hypertension is often associated with an inhibition of the vasa vasorum's vasodilator capacity resulting in intralamellar regions becoming hypoxic leading to the development of micro cracks, a credible antecedent of dissection [13,39–41]. Therefore, chronic hypertension may lead to a gradual reduction in the fracture resistance of arterial tissue. Cystic medial degeneration may also lead to localised reduction in the fracture strength of the aortic wall, resulting in initiation of delamination [42]. It is likely that some pathologies influence the fracture strength on a global scale, for example, connective tissue disorders significantly alter the inter-lamellar aortic microstructure through elastin deficiency (Marfan syndrome) and collagen deterioration (Ehler-Danlos syndrome) [43,44]. The incidence of arterial dissection is much higher in patients with connective tissue disorders such as Marfan syndrome and Ehler-Danlos syndrome [45–48]. Further mode II testing of excised pathological tissue is required to establish the effect, if any, of such pathologies on mode II fracture strength.

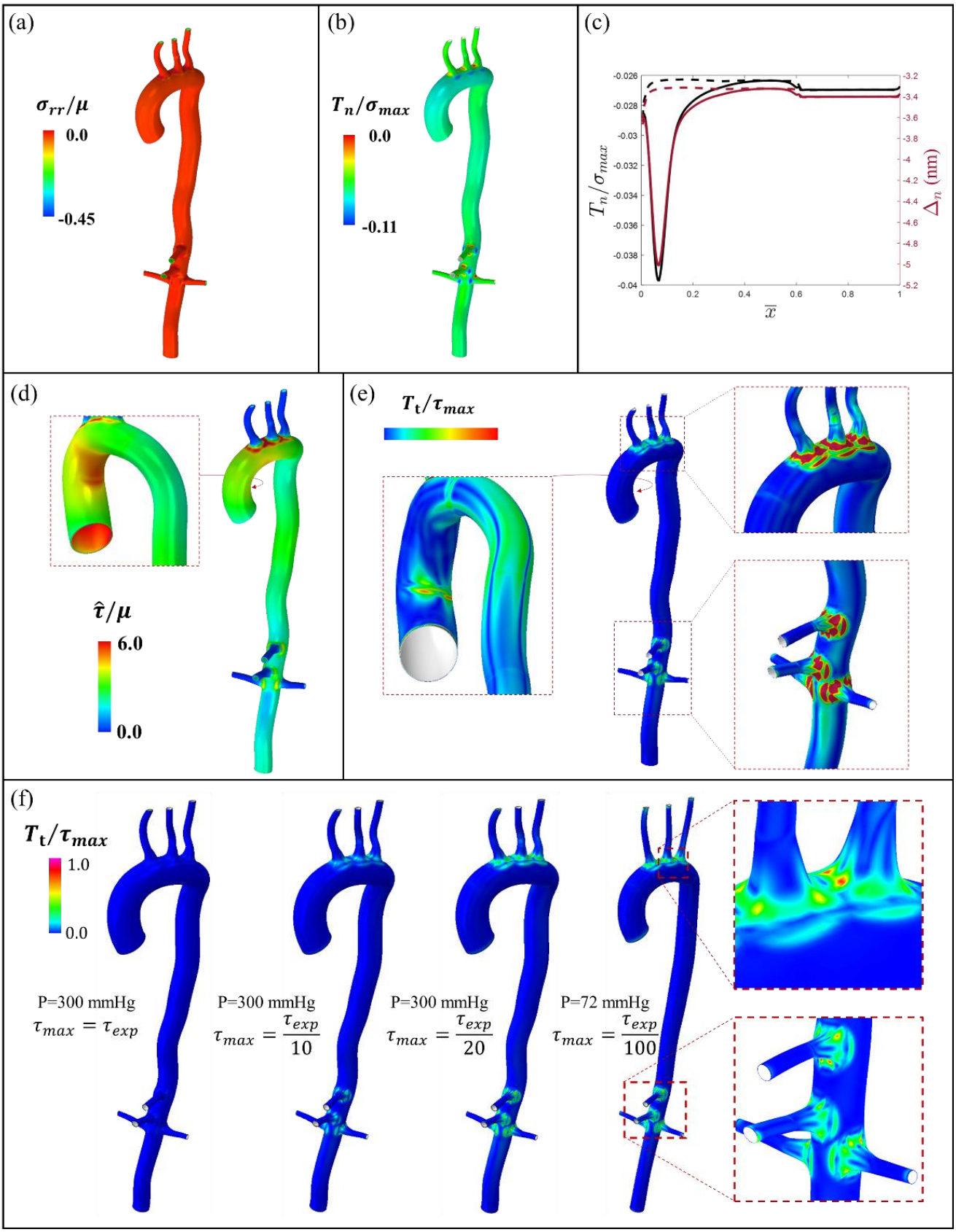

Figure 3. (a) contour plot of local radial compressive stress throughout the aorta under an applied pressure of 300 mmHg; (b) negative normal (compressive) tractions computed throughout the aorta under a pressure of 300 mmHg; (c) (left y-axis) normal traction along the inner and outer

curve of the aorta as a function of normalised length ($\bar{x}$); (right y-axis) normal separation Δ_n as a function of normalised length ($\bar{x}$), heavy penalisation of overclosure is observed. (d) Maximum local material shear stress ($\hat{\tau}$) in the aorta subject to a lumen pressure of 300 mmHg; (e) Shear tractions in the medial interface in the aorta subject to a lumen pressure of 300 mmHg. Detail windows show limit-adjusted contours highlighting regions of elevated shear traction; (f) Contour plots of shear traction (T_t) for four values of mode II interface strength (τ_{max}). τ_{exp} is the experimentally measured mode II fracture strength (1.6 MPa). Delamination is predicted to initiate if $T_t = \tau_{max}$. Applied lumen blood pressure (P) is indicated for all simulations.

3 Parametric investigation of the key factors that contribute to risk of vessel dissection

The results presented for the realistic subject-specific aorta model in Section 2 indicate that a significant reduction (100-fold) is required for spontaneous dissection initiation. In cases in which patients exhibit such reduced fracture strength of the aortic wall, additional anatomical features and physiological loading conditions may play an increased role in dissection risk. In the remainder of this study we perform a parametric assessment of the influence of a range of anatomical and physiological parameters on dissection risk, characterised by the computed shear traction distributions. Specifically, based on clinical evidence we investigate the following factors:

Material factors:

(i) Stiffness mismatch in the aortic wall in the radial direction. Chronic hypertension has been shown to induce hypoxic stiffening of the outer medial layer relative to the inner layer [12,49].

(ii) residual stress in the aorta wall. The opening angle of the aorta varies significantly as a function of aortic length, the influence of such heterogeneity of the residual stress field of the aorta on risk of dissection has not been previously quantified [50].

Physiological factors:

(i) cranial (axial) displacement has been previously documented as the primary displacement direction of the aortic root [51]. The role this displacement plays on shear tractions in the aorta has not been identified[1].

(ii) cardiac cycle displacement. The influence of the multiple simultaneous aortic root loading modes on AD risk has not been quantified previously.

Anatomical factors:

(i) Aortic wall thickness is known to increase as a result of hypertrophic remodelling due to chronic hypertension [49]. Aortic wall thickness may also increase in the presence of diseases such as giant cell temporal arteritis [52,53].

(ii) Aortic arch radius increases as does aortic length as the aorta ages [54].

(iii) Branching vessels are frequently involved in aortic dissection [55] and may spontaneously dissect even without the presence of aortic dissection [56,57].

The influence of all of the above factors on AD risk has not previously been quantified, either experimentally or computationally. Systematic analysis and insightful comparison of the above factors requires the construction of a regularised aorta model in which independent perturbation of a single parameter can be implemented. Additionally, parametric assessment of the influence of stiffness ratios through the aortic wall requires the implementation of linear material behaviour, rather than the complex anisotropic non-linear material behaviour used in our subject-specific model (Figure 3). In Section 3 we present the construction of a parameterised idealised aorta model and in Section 3.2 we present the key results of our extensive parametric investigations. Once again, it should be emphasised that the purpose of this component of our investigation is not

[1] A range of displacement modes were analysed (Figure 4(e)), however, for brevity cranial and cardiac cycle displacements are presented as the two most dominant displacement modes.

to create a realistic representation of the aorta (this has already been attempted in Section 2 above). Rather, the purpose of this systematic analysis is to gain fundamental insight into the relative influence of key parameters on the vessel stress state and dissection risk.

3.1 Development of an idealised and parameterised model of the aorta

In order to systematically quantify the contribution of aortic anatomical features on dissection risk, we construct an idealised series of parameterised geometries of the ascending aorta, aortic arch, and descending aorta. Given the evidence that AD primarily occurs between the elastic lamellar layers of the media [5,58], we assume the wall is a bi-layered composite; a cohesive zone model is applied at the interface between the two layers. Different material properties are assigned to each layer [13,59] in order to explore the influence of stiffness mismatch on interface tractions and dissection. Although the parameterised geometry is highly idealised and neglects branching vessels, such a parameterisation is necessary to quantitatively parse the contribution of each material/anatomical factor to AD risk.

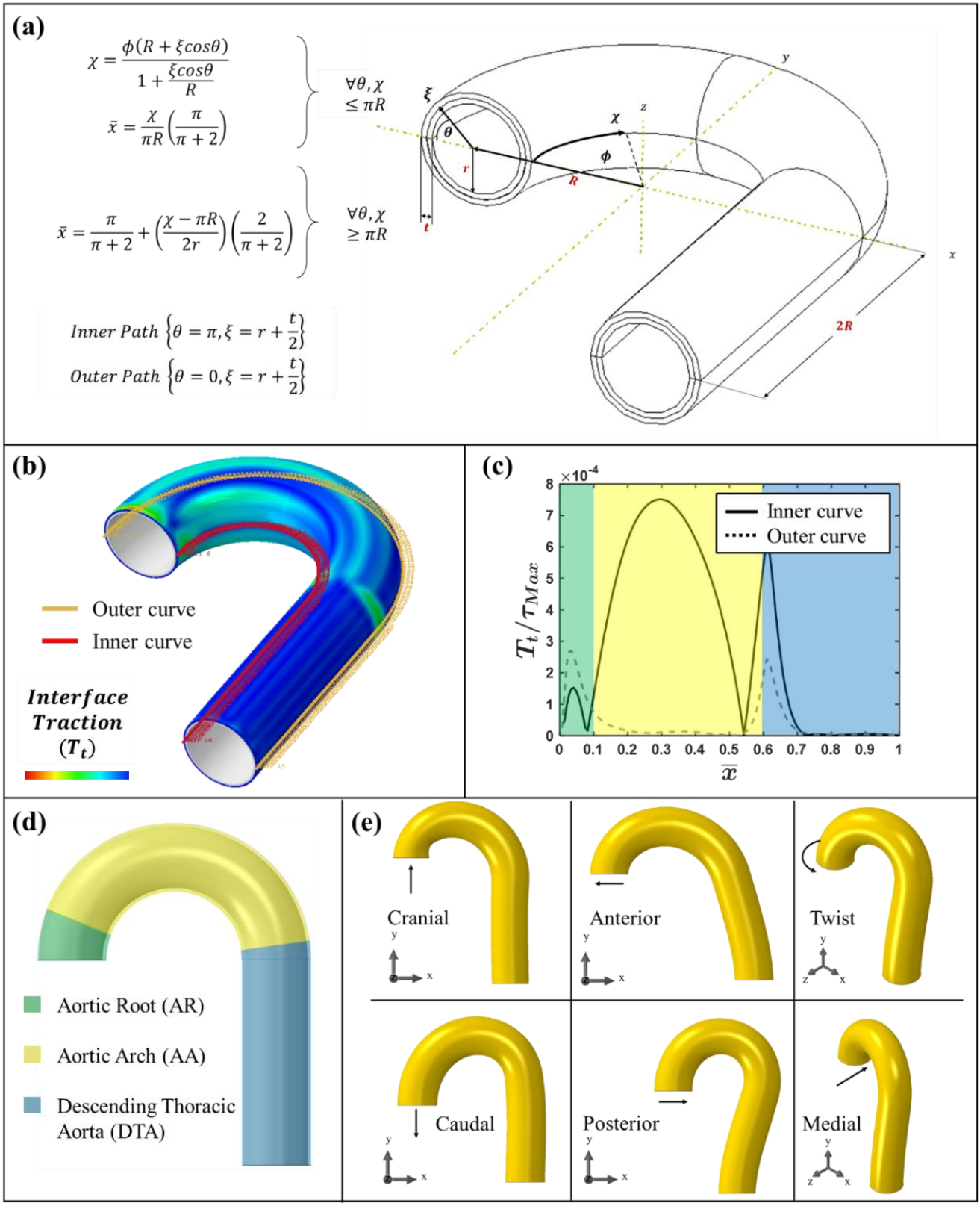

Figure 4. (a) Schematic representing the parameters in the model. The dimension $\chi(\phi, \theta, \xi)$ represents path length. $\bar{x}$ is the normalised path length $\forall(\theta, \xi)$; (b) contour plot illustration of the inner curve and outer curve on a representative geometry with interface traction shown; (c) illustration of traction plot along the inner and outer curves. Three colour coded regions are shown in (d); (e) illustrations of loading modes explored in the present study.

Anatomical parameterisation of idealised aorta: Figure 4 shows a schematic of the parameterised model. An interface path coordinate is defined (χ) which is a function of the angle ϕ, the local radial coordinate ξ, and the local circumferential angle θ, where the local system for $\chi \leq \pi R$ is distance R from the global origin. The interface path coordinate is then normalised to give the normalised path coordinate $\bar{x}$ (referred to as *normalised aortic length*). This allows for the description of an interface path in terms of the aortic arch $\chi \leq \pi R, \forall(\theta, \xi)$ and the descending thoracic aorta $\chi \geq \pi R, \forall(\theta, \xi)$.

Path lines are chosen such that the 'Inner' path runs along the section of highest curvature of the arch and continues in that plane through the descending thoracic aorta ($\theta = \pi, \xi = r + t/2$) (see Figure 4(b)). Path data is normalized according to each model geometry. Traction is computed at the path lines and plot as a function of the normalised path length ($\bar{x}$), as seen in the example traction plot in Figure 4(c). For convenience, we approximately describe the normalised length in terms of it anatomical location: aortic root (AR) $\approx 0 \leq \bar{x} \leq 0.1$, aortic arch (AA) $\approx 0.1 \leq \bar{x} \leq 0.6$, descending thoracic aorta (DTA) $\approx 0.6 \leq \bar{x} < 1$, see Figure 4(c-d).

Parameters varied in the models are as follows: arch radius (aortic curvature) (R), wall thickness (t), wall stiffness (E), stiffness discrepancy in the layers (E_i, E_o), and inner and outer layer thickness (t_i, t_o). The inner lumen radius (r) does not change and the outer lumen radius (r_o) changes with the thickness. The value range of geometric parameters for arch geometries are selected based on CT scan data. Values of arch radii and wall thickness are chosen in physiological [60], pathophysiological [52,53], and non-physiological ranges. In order to parse the influence of material stiffness mismatch between the two layers of the vessel we assume quasi-linear elastic neo-hookean material behaviour (non-linear hyperelastic material behaviour does not allow for the prescription of a constant stiffness ratio for a range of lumen pressures). Physiologically accurate non-linear anisotropic hyperelastic material behaviour is explored above in Section 2. Details of the cohesive zone formulation applied at the medial interface are presented in Section 2 above. Results of parametric studies are presented in terms of the following key non-dimensional groupings: t/r , R/r_o , E_i/E_o.

Physiological loading conditions and boundary conditions: Each model is created using a structured mesh of 8-noded quadrilateral first-order elements. To uncover the role of anatomical loading a variety of loading modes are investigated: caudal, cranial, anterior, posterior, mediolateral, and torsion (shown in Figure 4(e)). In order to accurately describe the physiological loading regime, displacement boundary conditions are based on ImageJ analysis of cine-MRI cardiac-cycle data [61]. Figure 5 shows an illustration of image analysis process in image J. Caudal-cranial motion and anterior-posterior motion is measured throughout the cardiac cycle at evenly spaced intervals. Extracted displacement data is normalised as a function of sinotubular junction (STJ) diameter and applied to the dimensions of the parameterised model as has been reported previously [17].

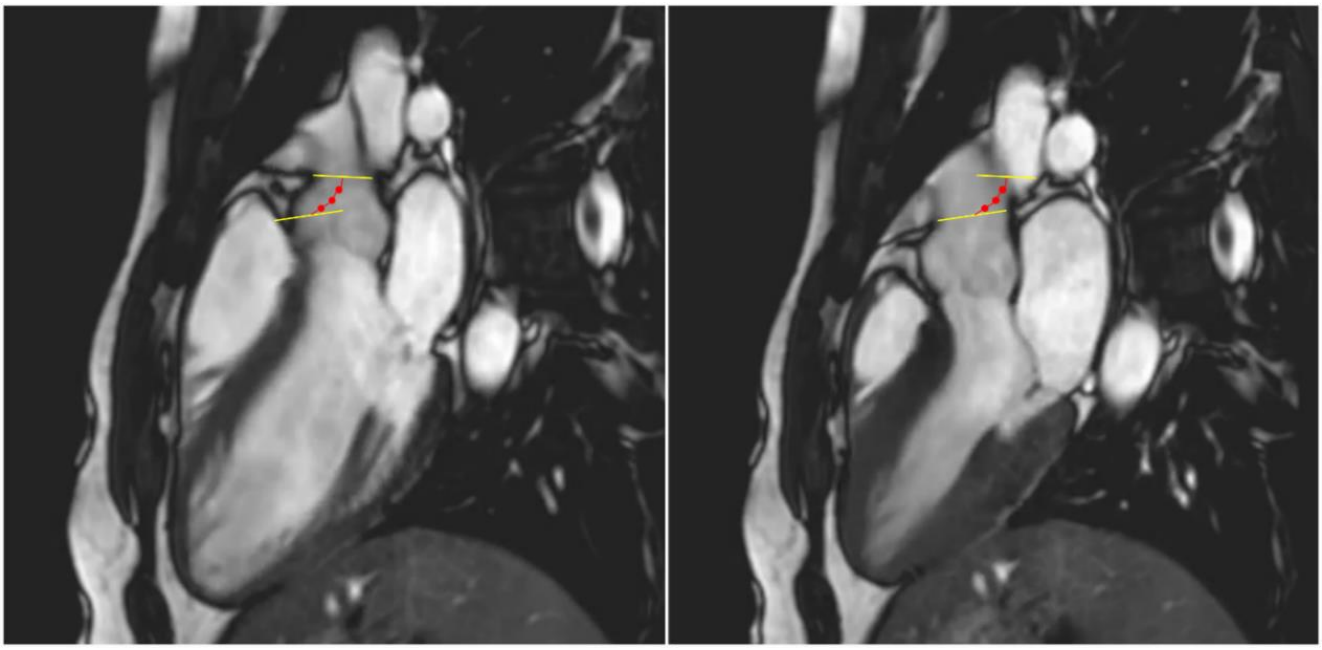

Figure 5. Cine-MRI image analysis. Yellow lines are in the same position in both images, illustrating the displacement of the aortic root. Red lines and circles show an example of the path

travelled by the aortic root.

Displacement boundary conditions are applied to the aortic root, while radial expansion due to applied lumen pressure is unconstrained. The aorta is constrained at the level of the mid-descending thoracic aorta, such that it remains planar with no axial displacement at this section (for $\overline{x} = 1.0$, $u_{zz} = 0 \ \forall\{\theta, \xi\}$), with only radial expansion and axial rotation being unconstrained at this section. In the case of applied loading due to cardiac movement, all transient displacements, rotations, and lumen pressures are applied at physiologically accurate magnitudes and timescales.

Development of a new approach to implement residual stress in aorta wall: A novel methodology is developed to include spatially varying residual stress in the aorta. Aortic ring geometries are created to match the desired geometries of the aorta. An overview of the process is described in Figure 6. Opening angle (γ) of the human aorta has been described previously as a function of normalised aortic length ($\bar{x}$) [50]. Residual stress can be estimated in artery through reversing the stress-free open-angle configuration to a closed residually stressed position (shown in Figure 6(a)). We perform closing angle simulations for the range of measured opening angles in the human aorta. The residual stress tensor is extracted as a function of radial coordinate (ξ) for each opening angle (local circumferential stress shown in Figure 6(a)). In order to apply the residual stress to the global aortic geometry, normalised aortic length ($\bar{x}$) and radial coordinate (ξ) are determined (Figure 6(b)). These dimensionless coordinates act as inputs to the residual stress tensor function (shown as the red lines in Figure 6(c)). The residual stress tensor is built using said inputs and transformed to the global coordinate system using the standard transformation shown in (d).

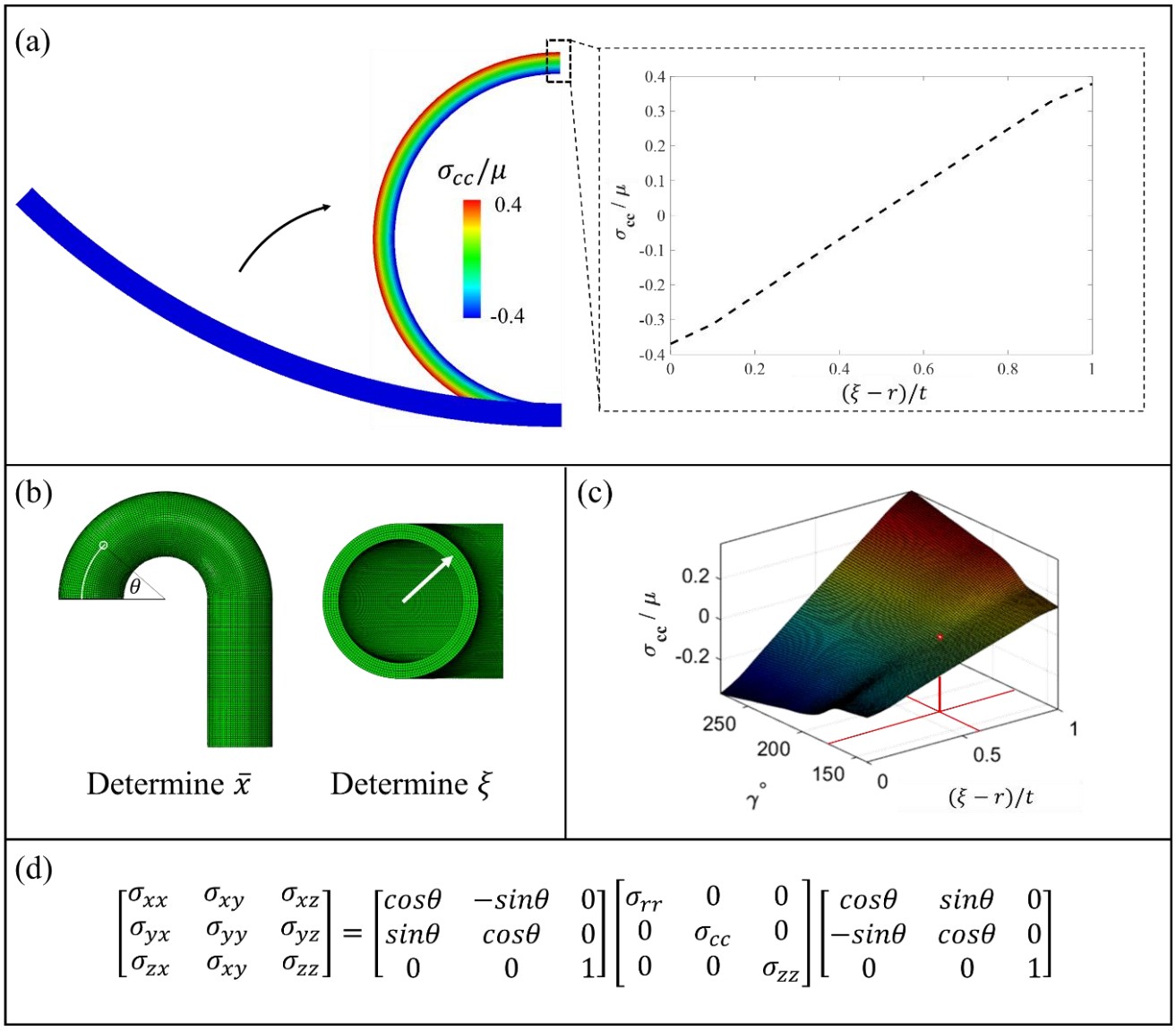

Figure 6. Overview of the residual stress methodology developed. (a) A series of opening-angle

aortic ring geometries are closed and the local stress tensors are recorded as a function of radial coordinate (ξ); (b) For each integration point, the normalised aortic length ($\overline{x}$) is determined as well as the radial coordinate (ξ); γ (which corresponds to $\overline{x}$) and ξ are inputs to the residaul stress function shown in (c); The local material residual stress tensor is then transformed into global coordinate (d).

Here we give a technical overview of the optimisation scheme: A MATLAB master function is developed which calls an objective function which calls and passes arguments to a python script. The python script opens the aortic ring model in Abaqus/CAE and updates the geometry, and any other model variables desired, based on the arguments from the objective function. The coordinates of the closed ring are imported using Matlab and the GIBBON toolbox to calculate the closed diameter and compare to the target diameter. Opening angle data of human aorta is evenly sampled at 10 points throughout the mean data-set for aortas aged over 60 years old [50].

Finite element models of the open equilibrated configuration of the aortic rings are created using the opening angle and an initial guess at the curvature of the open configuration. The artery is modelled as a bilinear hyperelastic anisotropic fibre-reinforced material. Symmetry is assumed, as such, half the circumference is modelled. A methodology that allows for the closing of a ring from any specified initial opening angle is developed and implemented. The opened equilibrated state of the aortic specimen is closed, and the closed diameter is compared to the target diameter in an optimisation scheme. The initial guess at the curvature of the opened segment is updated iteratively until the solution converges. When convergence is achieved for the first opening angle, the process is repeated for the next opening angle in the loop. When the loop of opening angles is complete the master MATLAB function calls a Python post-processing script which loops through each output database of the converged closing simulations. A *user-defined material behaviour subroutine (UMAT)* is developed to construct a residual stress tensor for each element based on its normalised aortic length, and radial coordinate. The full process is outlined in detail in the flowchart presented in Figure 7(a). The results of the closing angle simulations (Figure 7(b-c)) serve as input data to the user-defined subroutine.

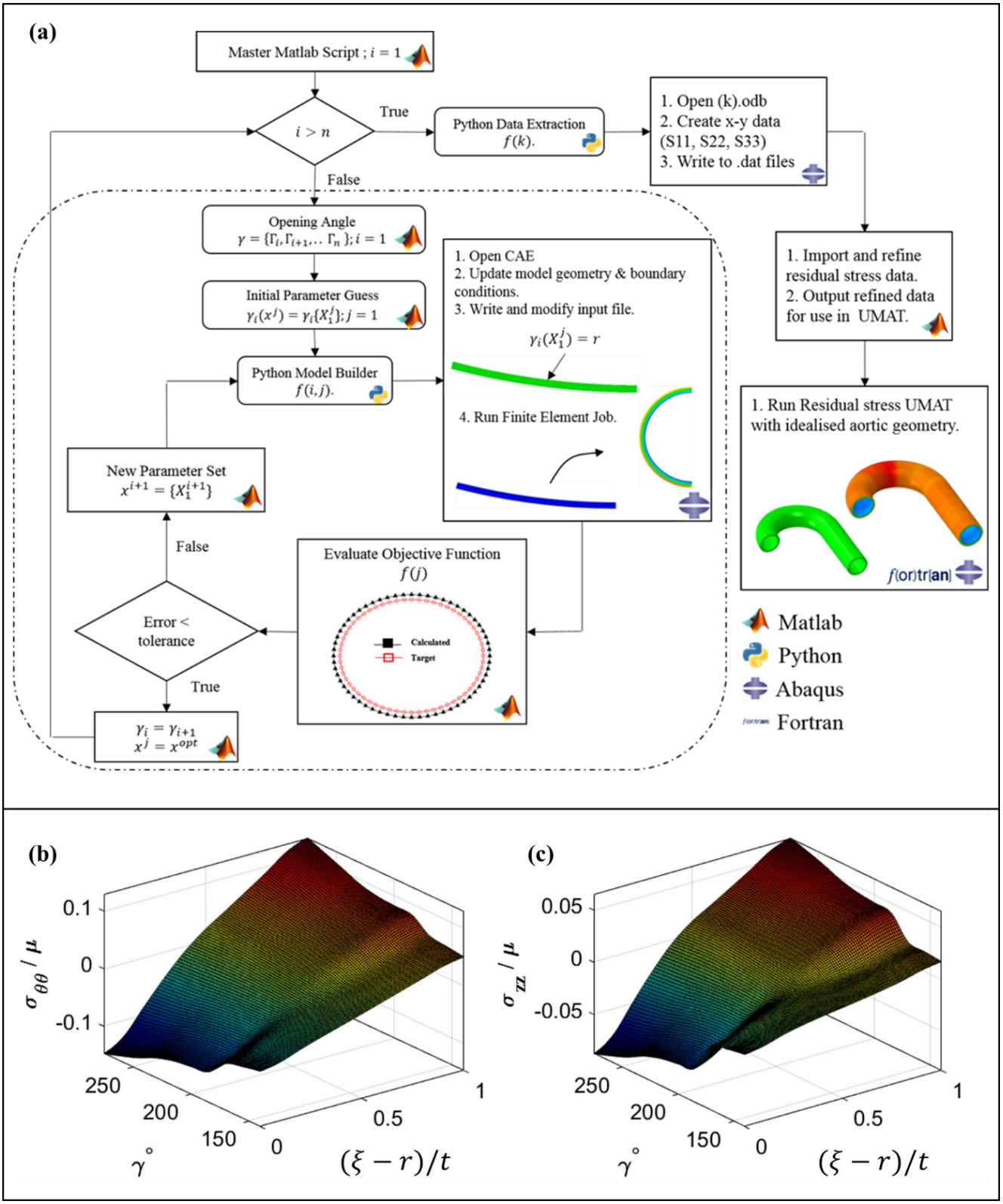

Figure 7. (a) Flowchart of the residual stress methodology; (b) circumferential stress as a function of opening angle γ and radial coordinate X_r/t; (c) axial stress as a function of opening angle γ and radial coordinate X_r/t.

3.2 Results of parametric analysis of key factors in aorta shear tractions and dissection

Results of our parameteric investigation are presented in three sections: *Material factors*; *Physiological loading factors*; *Anatomical factors*. Despite the parameterised and idealised vessel geometry, it will be noted that the traction state in the vessel wall is quite complex, with significantly different patterns of traction being computed in the root region, the arch region and the descending thoracic aorta. We present a series of contour plots, in addition to traction distributions along several anatomical paths, in order to illustrate the key features of each parameteric investigation. Unless otherwise stated, the following idealised model parameters are implemented: $\frac{t}{r} = 0.25, \frac{R}{r_0} = 3.0, \frac{E_i}{E_o} = 1$.

3.2.1 The influence of aortic material parameters on interface traction distribution

Bi-layer stiffness mismatch: In cases of severe hypertension unequal stiffening of the layers of the media occurs through hypoxia of the outer media due to restriction of blood flow from the vasa vasorum [13]. Figure 8 shows that for an applied cranial displacement, calculated tractions are highest when the stiffness mismatch in the bi-layer interface is highest. For layers of equal stiffness the peak tractions occur at the start of the DTA, however, increase in stiffness mismatch results in peak tractions at the AR. This may bear clinical relevance as arteriosclerosis is associated with chronic hypertension, aging, diabetes, obesity, high cholesterol, and smoking [2,4,9,62]. These findings suggest each of these risk factors (and any progenitor of arteriosclerosis) increase intramural tractions in the AR. While elevated intramural shear tractions contribute to the risk of dissection, in this case they are not sufficient to cause dissection.

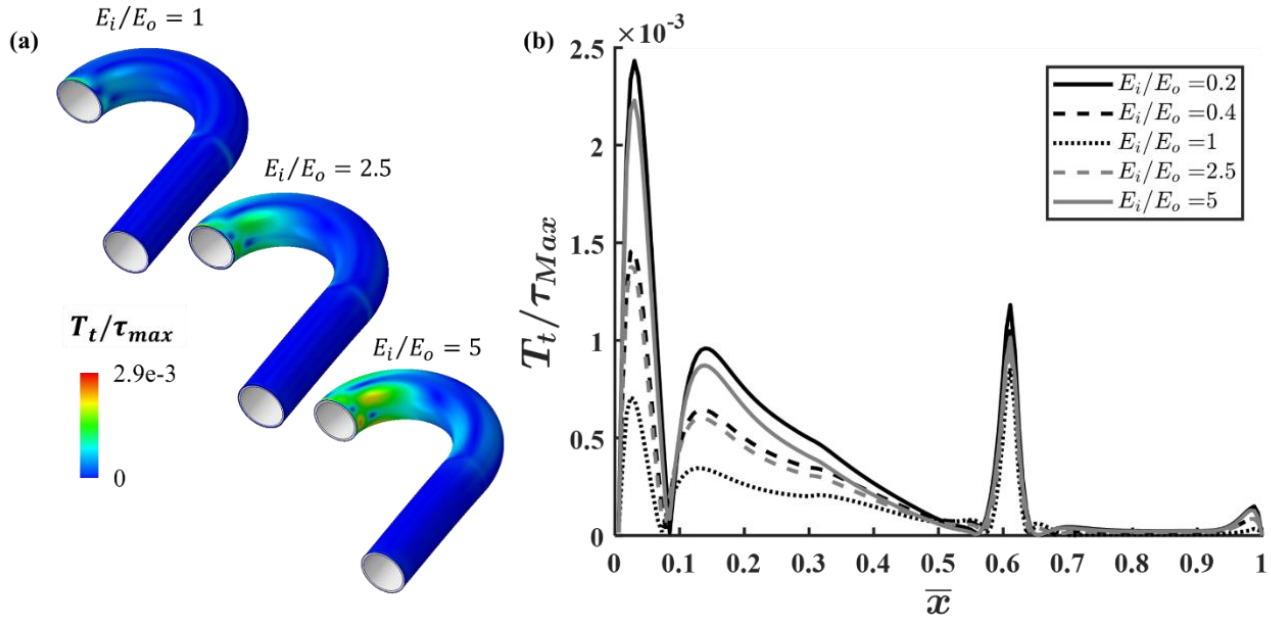

Figure 8. (a) T_t/τ_{max} contour plots for bi-layer stiffness mismatch for and an applied cranial displacement $\overline{V}/R = 0.275$ and $t/r = 0.25, R/r_o = 3.0$; (b) T_t/τ_{max} vs $\overline{x}$ for varying amounts of stiffness mismatch. Different parameter sets of E_i/E_o for a cranial displacement $\overline{V}/R = 0.275$ are investigated. $t/r = 0.25, R/r_o = 3.0$.

Residual stress: We next explore the influence of residual stress on AD risk. The opening angle of the human aorta has previously been measured and it has been shown that opening angle varies significantly as a funciton of aortic position [50]. The impact of such a heterogeneous residual stress state on AD risk has not been quantified previously. In Figure 9 we present the traction state of a residually stressed aorta and compare to a non-residually stressed aorta, both before and after the application of physiological loading conditions (systolic lumen pressure of 120 mmHg and cranial displacement of $\overline{V}/R \approx 0.2$). In the absence of physiological loading a highly heterogeneous distribution of residual circumferential stress is computed. However, the final stress state of the residually stressed aorta following the application of physiological loading is quite similar to that computed without the inclusion of residual stress. Essentially, heterogeneous residual stresses are approximately an order of magnitude lower than stresses generated by lumen pressure loading. The influence of residual stress on AD risk is

illustrated in Figure 9(b), showing computed shear traction along a path through the medial interface, both with and without inclusion of residual stress. While residual stress results in slight increases in peak tractions, computed values remain two orders of magnitude lower than the experimentally measured mode II interface strength (1.6 MPa).

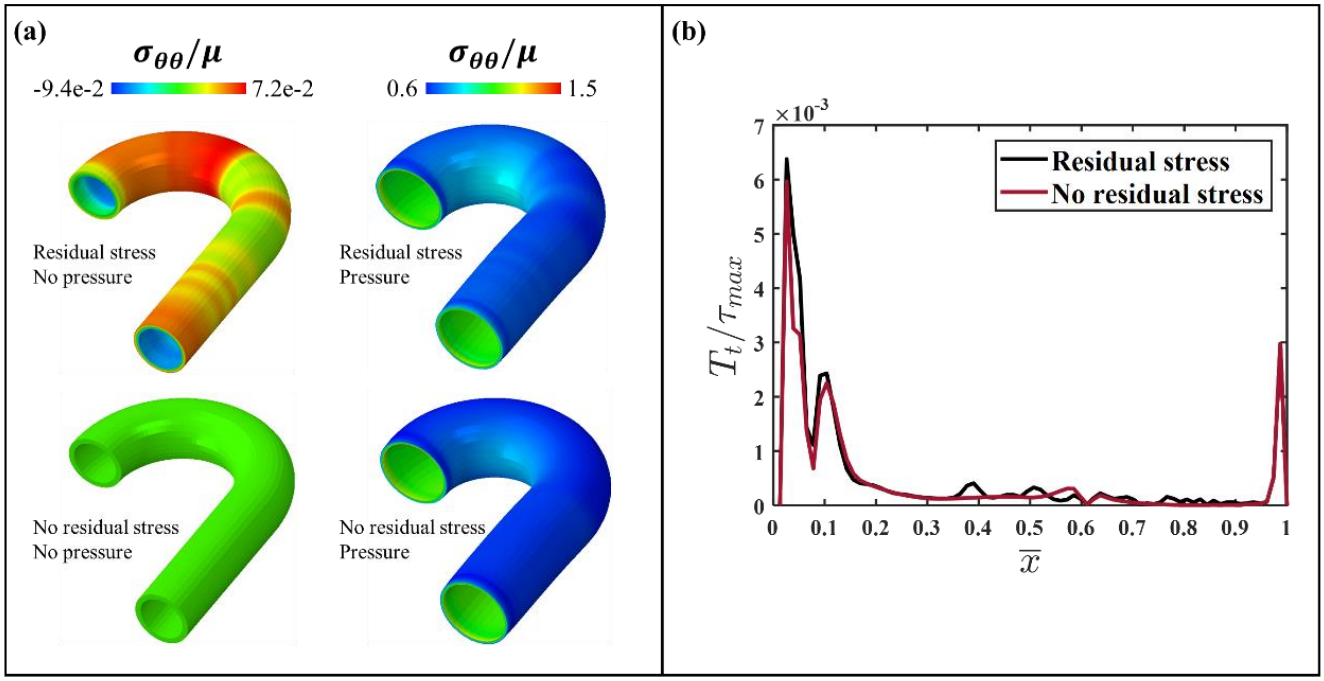

Figure 9. (a) Comparison of local circumferential stress distribution, both with and without inclusion of residual stress. Both zero applied loading and physiological applied loading (120 mmHg lumen pressure and $\overline{V}/R \approx 0.2$) are considered. (b) Computed shear traction along a path through the medial interface, both with and without inclusion of residual stress.

3.2.2 Influence of physiological and super-physiological loading on interface tractions

Here we examine the influence of a range of physiological boundary conditions on the AD risk. Although all of the loading modes listed in Figure 4(e) are examined, for brevity we focus on two predominant loading modes: cranial displacement and anterior displacement.

Anterior aortic root displacement: Figure 10(a) shows a series of contour plots demonstrating increasing traction with increasing applied anterior displacement at the aortic root ($\overline{V}/R$). High traction concentrations are computed in the AR. Figure 10(b) shows shear traction as a function of $\bar{x}$ for each recorded anterior displacement of the aortic root.

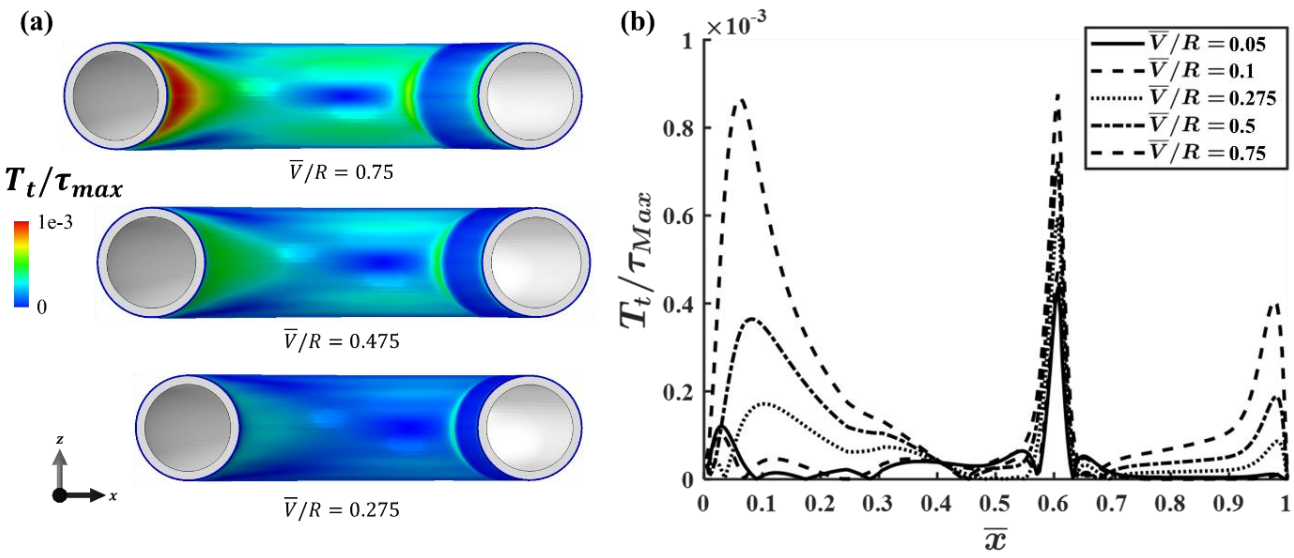

Figure 10. (a) T_t/τ_{Max} evolution with increasing anterior displacement ($\overline{V}/R$) and (b) T_t/τ_{Max} as a function of $\overline{x}$ for an arch of $R/r_o = 3.0, t/r = 0.25$ for increasing anterior displacement.

Cranial aortic root displacement: As shown in Figure 11, simulations predict maximum tractions for highest values of cranial displacement. Average axial displacement of the aortic root has been observed to be $8.9 \pm 1.8mm$ [17], corresponding to $\bar{V}/R = 0.297 \pm 0.06$. Traction concentrations are computed in the AR, with similar concentrations computed at the start of the DTA. Increasing displacement has a near linear effect on the peak traction at $\overline{x} = 0.6$, whereas the effect in the AR is highly non-linear. The traction state in the DTA is insensitive to changes in displacement. This is not surprising as only 1.3% of AD are reported to initiate in the infrarenal aorta [63]. These findings suggest that a possible contributing factor for lower incidences of abdominal dissection may be the significantly lower intramural tractions present in the infrarenal aorta relative to the aortic arch.

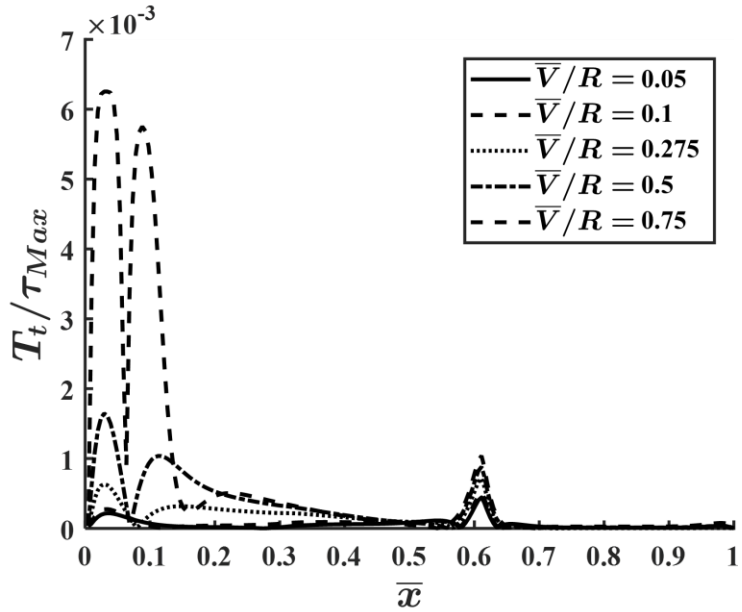

Figure 11: T_t/τ_{Max} on the inner curve vs. $\overline{x}$ for the simulated range of values of cranial displacement ($\overline{V}_{CRANIAL}/R$) of an arch with parameters $R/r_o = 3.0, t/r = 0.25$.

Combined Caudal/Cranial, Anterior/Posterior displacement: Here we examine the influence of the full cardiac cycle on the risk of dissection. Figure 12(a) shows the contour plots of shear traction near the aortic root during key timepoints in the cardiac cycle where the tangential tractions are highest. As shown in Figure 12(a) at timepoint (a) (ventricular ejection) there is a small traction concentration near the aortic root on the inner curve and two larger concentrations in the centre of the arch ($\bar{x} = 0.3$) either side of the inner curve. Figure 12(b) reveals that, for timepoint (b) (maximum aortic systole), the peak shear stress tractions are increased in magnitude and area compared to the timepoint at which the aortic valve opens. This is the point in the cardiac cycle with the maximum calculated tractions.

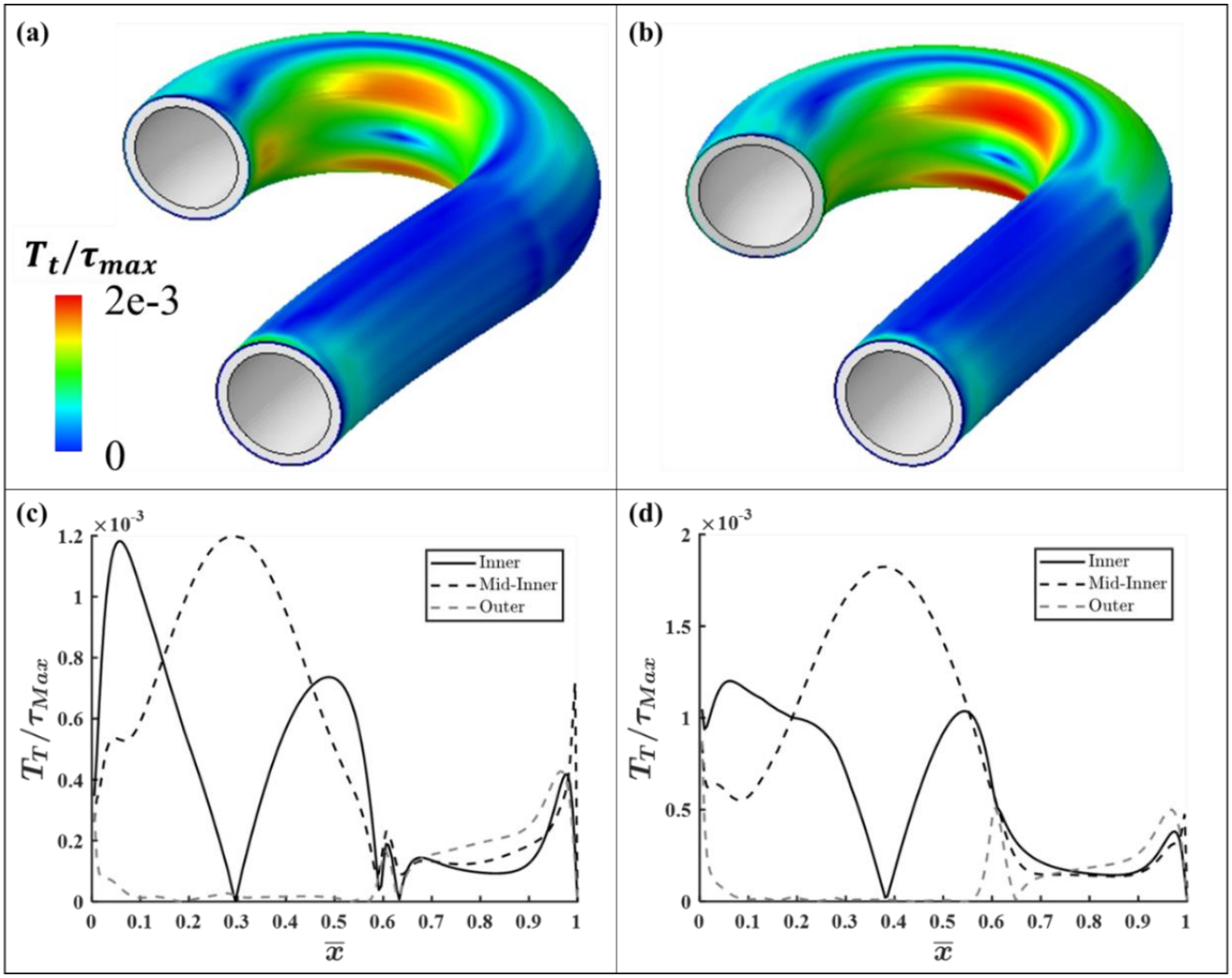

Figure 12. (a) T_t/τ_{Max} contour of the aortic arch during ventricular ejection with parameters $R/r_o = 3.0, t/r = 0.25, P_{Lumen} = 80mmHg$; (b) T_t/τ_{Max} contour of the aortic arch during max aortic systole ($P_{Lumen} = 120mmHg$); (c) T_t/τ_{Max} as a function of $\overline{x}$ for simulation presented in (a) along the Inner, Outer and Mid-Inner curves ($\theta = \pi, \theta = 0, \theta = \pi/4$ respectively); (d) T_t/τ_{Max} as a function of $\overline{x}$ for simulation presented in (b) along the Inner, Outer and Mid-Inner curves.

In Figure 13 we present a summary and comparison of the effect of each loading mode on AD risk in terms of computed shear traction (T_t/τ_{max}). A luminal pressure of 200 mmHg causes a peak in shear traction greater than any loading mode other than cranial displacement. Pressure loading does not result in traction concentrations in the AR but does in the DTA. Cranial causes the highest tractions, mainly in the AR. It can be seen from this figure that the stress state in the aorta is highly complex and that all physiological loading modes result in tractions approximately three orders of magnitude below τ_{max}. The effects of disease on aortic root displacement has not been investigated in great detail in the literature, however one study has noted decreased axial displacement (caudal/cranial) as a result of aortic valve regurgitation which in theory should

reduce intramural traction [51]. The findings of this study, however, suggest that aortic root motion, both physiological and pathophysiological, does not produce sufficient traction to result in initiation of dissection.

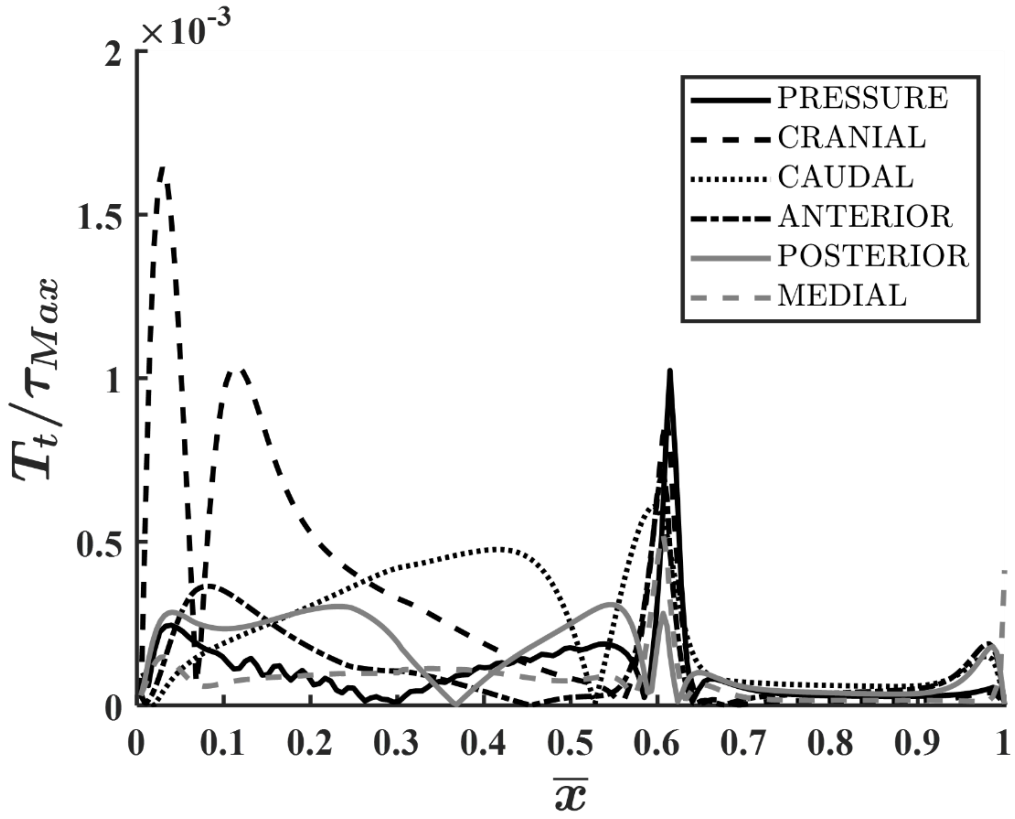

Figure 13: T_t/τ_{Max} as a function of $\overline{x}$ along the inner path for an arch of $R/r = 0.3, t/r = 0.25$ for a displacement equal to $\overline{V}/R = 0.5$ for each loading mode, also included is a lumen pressure of 200mHg with no aortic root diplacement.

3.2.3 Influence of geometric anatomical factors on interface tractions

Wall thickness: Increased wall thickness is a known result of chronic hypertension [15,16] and also a known symptom of giant cell temporal arteritis [53]. Both, chronic hypertension and giant cell arteritis are known risk factors of AD [3,64]. These risk factors may be linked through some underlying mechanical basis, which we explore in Figure 14. The influence of aortic wall thickness on the shear traction in the inner and outer curve of the vessel is investigated by applying cranial displacement at the root of the arch. As shown in Figure 14, a higher value of wall thickness results in higher shear traction. The traction along the inner curve of the arch varies significantly, depending on the wall thickness. Peak tractions occurs along the inner curve at the centre of the arch ($\bar{x} \approx 0.3$) reaching a value of $T_t/\tau_{Max} = 7.5\text{e-}4$ when $t/r = 1$. The location of peak tractions aligns with the clinical observation that approximately two thirds of ADs occurr in the ascending aorta and aortic arch (when $0.0 \leq \bar{x} \leq 0.6$) [3,4,65]. Additional traction localizations are computed at $\overline{x} = 0.6$ at the start of the DTA. Traction is near-zero in the DTA ($\overline{x} > 0.7$) regardless of wall thickness. Contour plots of shear traction distriutions throughtout the medial interface are shown in Figure 14(b) and Figure 14(c). Only half-wall thickness shown in order to expose the medial interface.

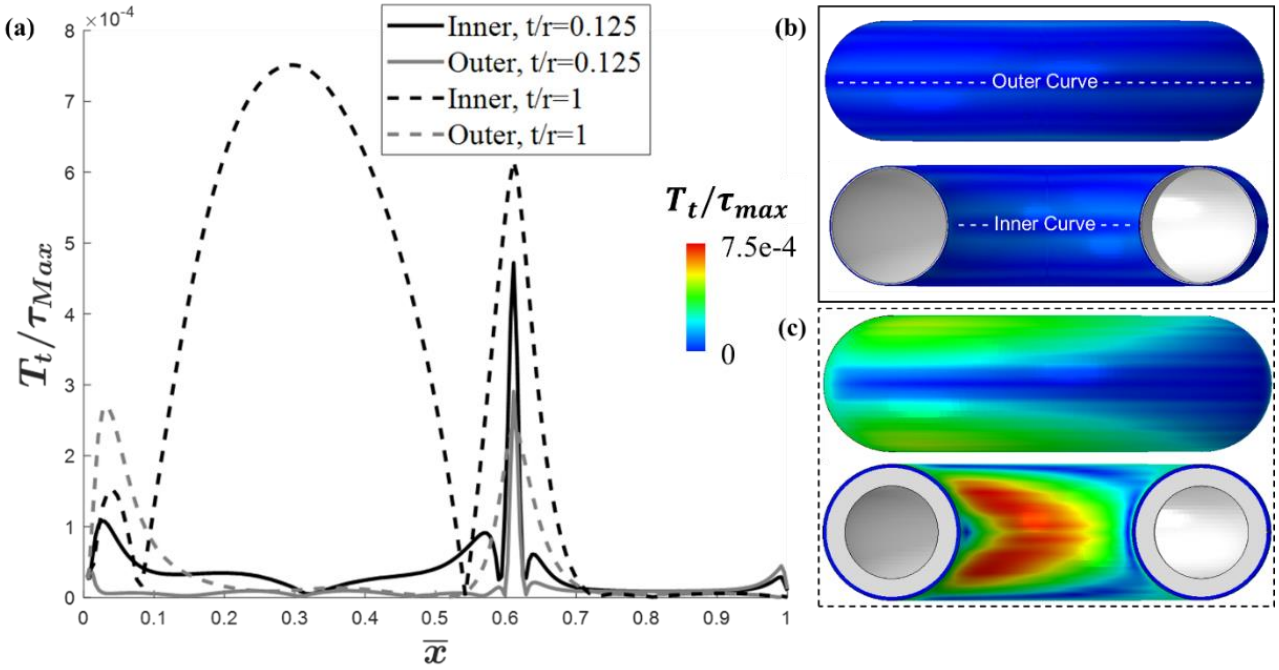

Figure 14. (a) Normalised shear traction (T_t/τ_{max}) as a function of normalised aortic length ($\overline{x}$) for an applied cranial displacement at the aortic root ($\overline{V}_{Cranial}/R = 0.05$) for $t/r = 1$ and $t/r = 0.125$. Path data is taken from the Inner and outer curves. The contour plots (b) and (c) show the distribution of (T_t/τ_{Max}) on the interface for $t/r = 0.125$ and $t/r = 1$, respectively.

These findings suggest that wall thickness significantly influences the traction state in the aorta. However, even for extremely thick vessel walls computed tractions are significantly lower than the mode II strength of the aorta. As an example, even if the wall thickness is the same as the wall thickness in a severe case of giant cell temporal arteritis [52] ($t/r = 1$) and an applied physiological displacement results in tractions 1000 times smaller than the mode II strength of a healthy artery. Therefore, an increase in wall thickness alone, without a corresponding reduction in fracture strength will not result in spontaneous AD. Interestingly, aortic wall thickness decreases in patients with Marfan syndrome (who are more at risk to suffer an AD), our results suggest this would decrease the intramural tractions in the aorta and risk of AD [66]. Wall thinning may be an adaptive response to counteract the increased AD likelihood due to a reduced fracture toughness (due to connective tissue disorder).

Arch radius: An increase in aortic arch radius occurs naturally with age. Similarly, an increase in aortic length occurs with age [54]. The influence of these anatomical changes on the AD risk has not previously been investigated. As shown in Figure 15, a lower arch radius results in a higher traction at the medial interface. Maximum tractions are computed in the configuration with the lowest arch radius ($R/r_o = 1.25$) with significant peaks predicted in the centre of the arch and at the DTA. Figure 15(b) shows the magnitude of the shear traction for each configuration of arch radius along the inner path of the aorta for an anterior displacement $\overline{V} = 0.15r_o$. Peak tractions are predicted in the centre of the arch along the inner curve.

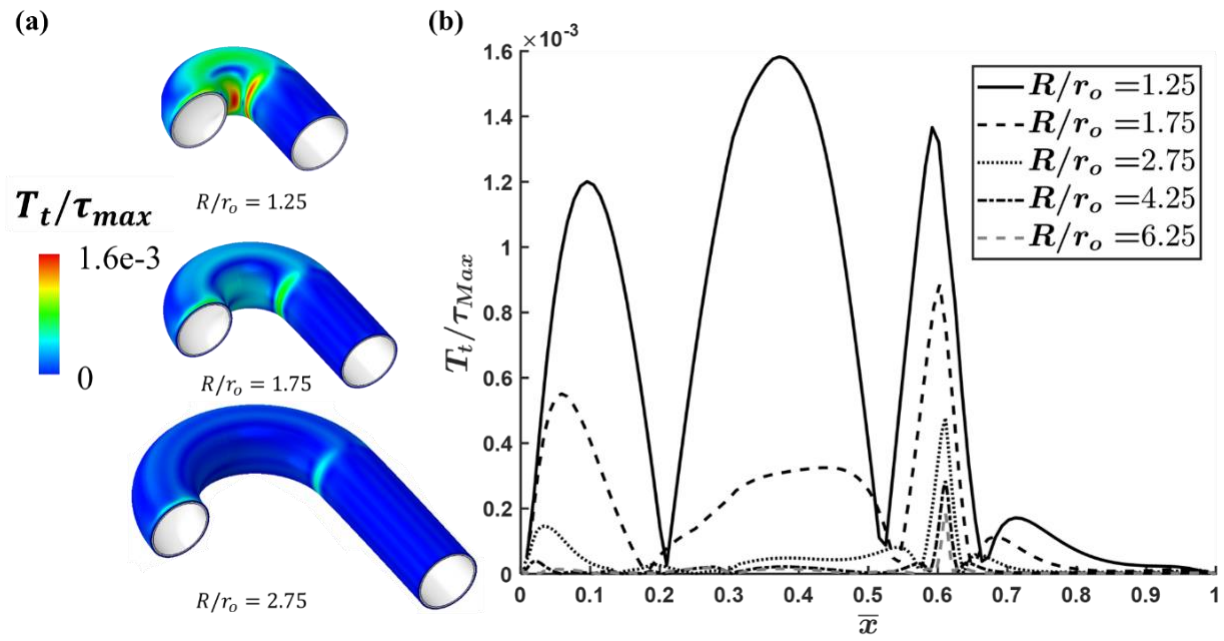

Figure 15. (a) Contour plot of normalised shear traction (T_t/τ_{Max}) for arch radius configurations $R/r_o = 1.25$, $R/r_o = 1.75$, and $R/r_o = 2.75$ for an applied anterior displacement $\overline{V} = 0.15r_o$; (b) T_t/τ_{Max} along the inner curve as a function of $\overline{x}$ for each configuration of R/r_o where $t/r = 0.25$.

A known implication of the increase in radius of the aortic arch with age is a reduced risk of aortic transection following rapid deceleration (as typically experienced in road traffic accidents) [67]. The primary cause of transection in younger patients is generally purported to be due to the restraint (and consequent stress concentration) of the ligamentum arteriosum at the aortic isthmus [68]. The analyses presented in the current study suggest a secondary cause: the younger aorta, with a lower arch radius, is more prone to intramural delamination in blunt trauma due to higher interface tractions. Specifically, as shown in Figure 15, for the case of a low arch radius ($R/r_o = 1.25$) peak tractions of $T_t/\tau_{max} = 1.6\text{e-}3$ occur in the aortic arch at $\overline{x} = 0.1$ and $\overline{x} = 0.4$. The current analysis suggests that the increase of the radius of the aortic arch as part vessel remodelling with increasing age leads to a reduction in shear tractions along the medial interface, with a consequent reduction in AD risk. However, it should be noted age related pathophysiological remodelling of the vessel also entails an increase in vessel stiffness [9] and thickness [48], and both effects have been shown (Figure 8 and Figure 14, respectively) to increase shear tractions and AD risk.

Finally, and most importantly, it should be noted that even for the smallest arch radius simulated in Figure 15, the computed shear tractions along the medial interface are 3 orders of magnitude lower than the mode II strength of healthy tissue.

Branch vessels: In order to investigate the role of ostia and branching vessels, idealised geometries containing supra-aortic vessels are also created using the GIBBON toolbox in MATLAB [69]. The supra-aortic vessels represent the brachiocephalic, the left common carotid, and the left subclavian arteries (seen in Figure 16(a)). Figure 16 shows the effect of branching vessels on the shear traction distribution in the aortic arch under a luminal pressure load of 120mmHg. Significant traction concentrations are computed at the ostia of the brachiocephalic, the left common carotid, and the left subclavian arteries. The presence of supra-aortic vessels significantly increases the tractions in the arch. However, these tractions are approximately two orders of magnitude lower than the mode II fracture strength of healthy tissue and as such are insufficient to cause dissection.

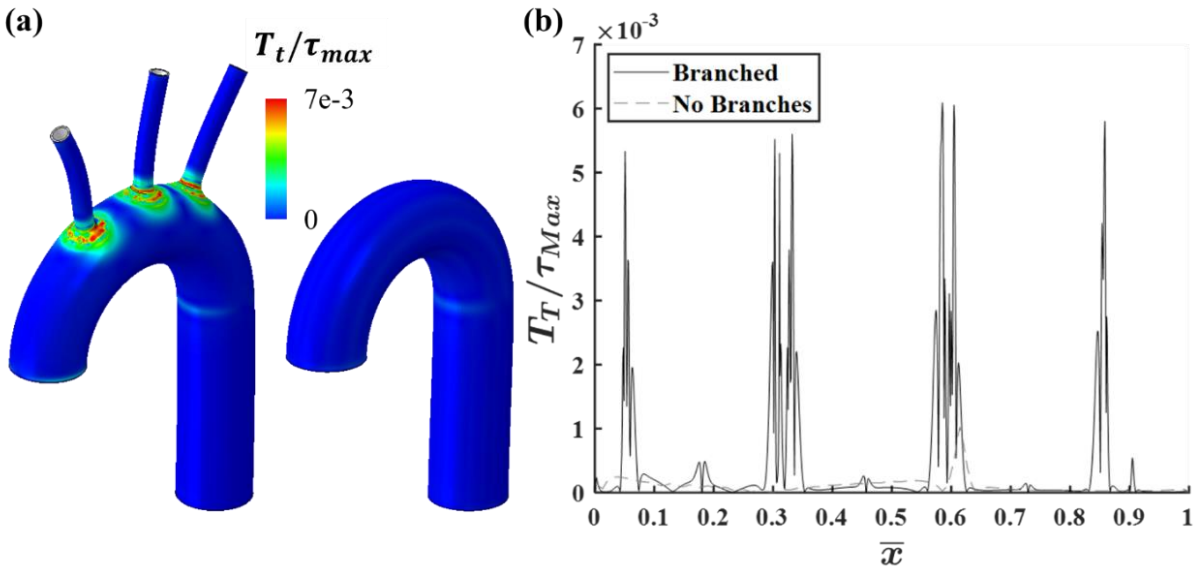

Figure 16. (a) Contour plot showing T_t/τ_{Max} of the aortic arch with and without supra-aortic branches for lumen pressurisation to 120mmHg; (b) T_t/τ_{max} vs $\overline{x}$ along the outer curve of the aorta ($R/r = 3.0, t/r = 0.25$) with and without branches.

3.2.4 Will a dissection propagate a long distance if interface strength is reduced?

In order to further examine the conditions for spontaneous AD initiation and crack propagation, a series of simulations are performed using reduced values of mode II fracture strength along the medial interface, shown in Figure 17. Specifically, interface strengths that are 100, 1000, and 10000 times lower than the healthy value of τ_{exp}=1.6 MPa are implemented. In all cases a physiological lumen pressure of 120 mmHg is applied and physiological ($\bar{V}/R = 0.5$) and super-physiological ($\bar{V}/R = 0.75$) cranial displacement are applied. Predicted regions of interface delamination are shown in Figure 16(a). In the case of a 100-fold reduction in fracture strength localised dissection is predicted at the AR only for the case of super-physiological cranial displacement. A 10000-fold reduction in interface strength must be implemented in order to computed extensive delamination throughout the entire region of the aortic arch. Simulations performed using a previously developed viscoplastic cohesive zone model require a similar level of reduction in interface strength to predict corresponding patterns of dissection.

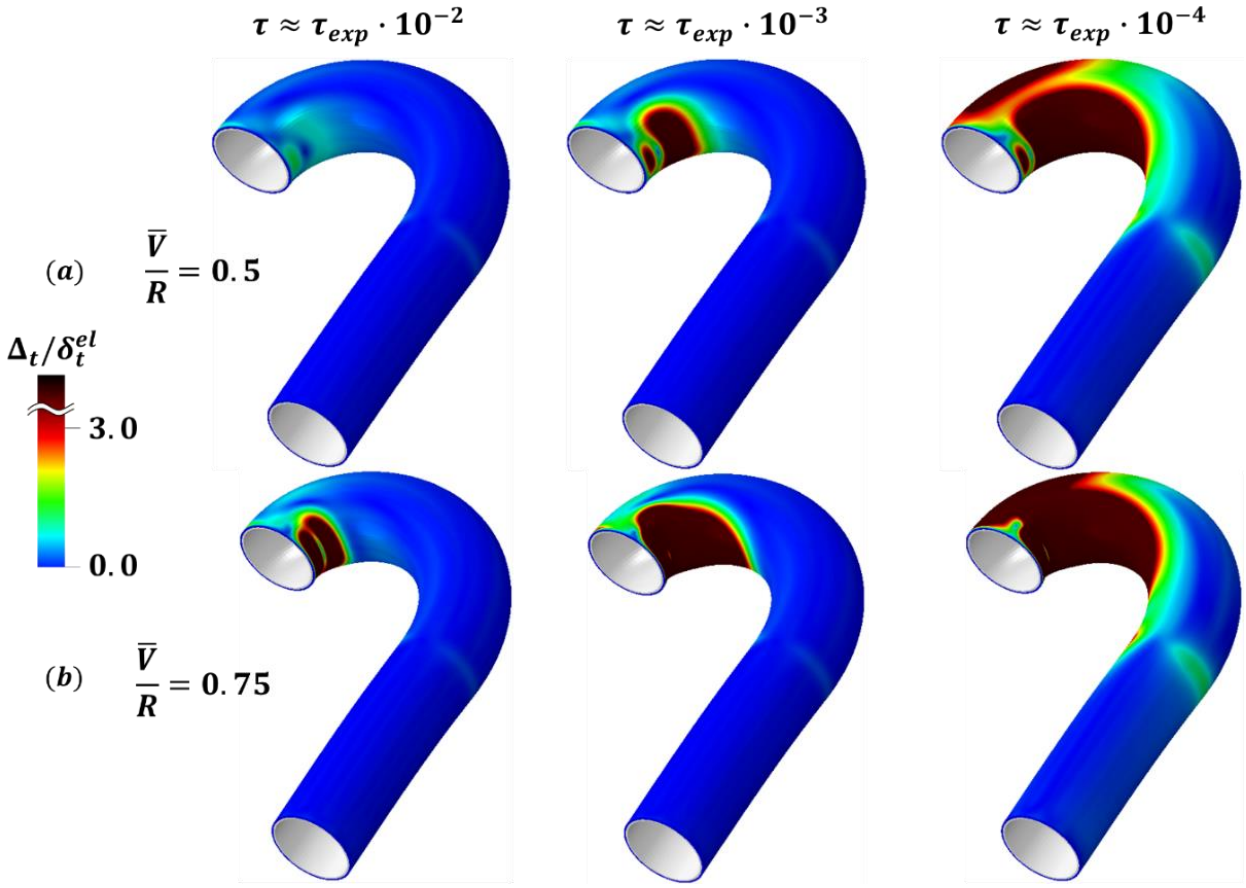

Figure 17. Computed regions of delamination (red + black contours) computed for three interface strengths, all of which are significantly $(100, 1000, 10000$ times) lower that the experimentally measured interface strength of a healthy intact aorta (τ_{exp}). A computed interface separation of $\Delta_t/\delta_t^{el} \geq 3$ indicates full damaged delamination. A physiological lumen pressure of 120 mmHg and a cranial displacement of the arch $(R/r = 3.0, t/r = 0.25)$ are applied. (a) Interface delamination for a cranial displacement of $\bar{V}/R = 0.5$; (b) interface delamination for a cranial displacement of $\bar{V}/R = 0.75$.

4 Concluding remarks

Parametric investigations reveal that shear tractions along the medial interface are increased by the following factors: Increased stiffness mismatch in the vessel wall due to hypoxic stiffening of the outer media; increased wall thickness; decreased arch radius. Simulations also suggest that residual stress (as characterised by the vessel opening angle) does not significantly increase shear tractions along the medial interface. Significant concentrations of shear traction are computed near to branching vessels. Cranial movement of the AR during the cardiac cycle leads to higher values of tangential traction in comparison to anterior and caudal movements. However, while all of the aforementioned parameters will result in increased interface tractions, it should be noted that even extreme pathophysiological loading, or pathological anatomical remodelling is shown to result in elevated shear tractions that are at least two orders of magnitude lower than the experimentally measured mode II shear strength of healthy aortic tissue. Simulations suggest that a 100-fold decrease in shear fracture strength is required to result in spontaneous dissection initiation at the AR, without extensive propagation. In order to simulate extensive propagation of a dissection throughout the arch (as reported clinically [3]) our simulations suggest that the mode II strength of the aorta must be reduced by a factor of 10^{-4}. This suggests that a significant phase change of the aortic tissue occurs prior to AD.

Other methods such as extended finite element method (XFEM) and element removal may be used to model fracture when the crack path is unknown [70,71], however, given the fracture observed in AD occurs primarily in the circumferential-axial plane cohesive zone modelling is used in the present study. Recent J-integral analyses reveal this fracture occurs in the circumferential-axial plane due to significant toughening against radial crack growth due to the highly aligned collagen fibres

behind the crack tip [30]. Pre-existing luminal injury or damage in the form of an intraluminal tear is not considered in the present study, nor is a pre-existing dissection with a patent false lumen. These are the subject of ongoing investigation and will be presented in a follow-on study. Future models examining AD risk may also consider active contractility of smooth muscle cells, fibroblasts, and endothelial cells using active contractility formulations [72,73].

5 Appendix A: Mesh Convergence

Here we present the mesh convergence study for the parameter study model. Convergence is achieved for the mesh with ≈ 93,000 elements. All simulations are performed for these number of elements.

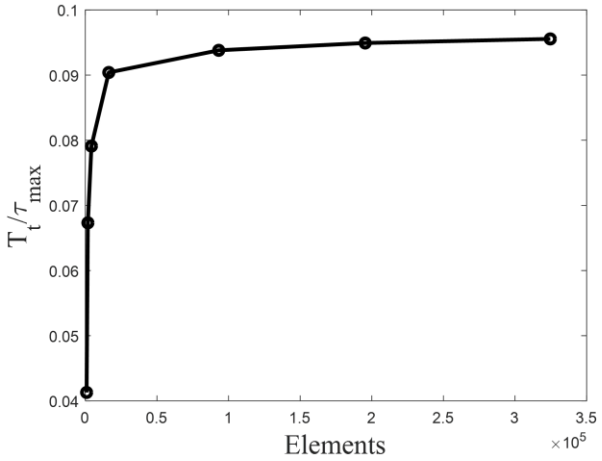

Figure 18: Variation of the normalised shear traction at $\bar{x} = 0.6$ verses the number of elements in the mesh.

6 References

1. Wang DS, Dake MD. Endovascular therapy for aortic dissection. In: *Thoracic Aortic Diseases*. Springer Berlin Heidelberg; 2006:189–198.

2. Mészáros I, Mórocz J, Szlávi J, et al. Epidemiology and clinicopathology of aortic dissection: A population- based longitudinal study over 27 years. *Chest* 2000; **117**(5):1271–1278. doi:10.1378/chest.117.5.1271.

3. Hagan PG, Nienaber CA, Isselbacher EM, et al. The International Registry of Acute Aortic Dissection (IRAD). *The Journal of American Medical Association* 2000; **283**(7):897–903. doi:10.1001/jama.283.7.897.

4. Criado FJ. Aortic dissection: a 250-year perspective. *Texas Heart Institute journal / from the Texas Heart Institute of St. Luke's Episcopal Hospital, Texas Children's Hospital* 2011; **38**(6):694–700.http://www.pubmedcentral.nih.gov/articlerender.fcgi?artid=3233335&tool=pmcentrez&rendertype=abstractAccessedJanuary 5, 2016.

5. Gasser TC, Holzapfel GA. Modeling the propagation of arterial dissection. *European Journal of Mechanics, A/Solids* 2006; **25**(4):617–633. doi:10.1016/j.euromechsol.2006.05.004.

6. Fuster V, O'Rourke RA, Walsh R, Poole-Wilson P. *Hurst's the heart*. McGraw Hill Professional; 2007.

7. Murai T, Baba M, Ro A, et al. Sudden death due to cardiovascular disorders: a review of the studies on the medico-legal cases in Tokyo. *The Keio Journal of Medicine* 2001; **50**(3):175–181. doi:10.2302/kjm.50.175.

8. Clough RE, Nienaber CA. Management of acute aortic syndrome. *Nature reviews. Cardiology* 2015; **12**(2):103–14. doi:10.1038/nrcardio.2014.203.

9. Greenwald SE. Ageing of the conduit arteries. *Journal of Pathology* 2007; **211**(2):157–172.

10. Rorive GL, Carlier PG. Hypertension and the arterial wall. *Acta Clinica Belgica* 1983; **38**(6):353–359.http://www.ncbi.nlm.nih.gov/pubmed/7036052AccessedJune 21, 2017.

11. Arribas SM, Hinek A, González MC. Elastic fibres and vascular structure in hypertension. *Pharmacology and Therapeutics* 2006; **111**(3):771–791. doi:10.1016/j.pharmthera.2005.12.003.

12. Laurent S, Boutouyrie P, Lacolley P. Structural and genetic bases of arterial stiffness. *Hypertension* 2005; **45**(6):1050–1055.

13. Angouras D. Effect of impaired vasa vasorum flow on the structure and mechanics of the thoracic aorta: implications for the pathogenesis of aortic dissection. *European Journal of Cardio-Thoracic Surgery* 2000; **17**(4):468–473. doi:10.1016/S1010-7940(00)00382-1.

14. Henrichs KJ, Unger TH, Berecek KH, Ganten D. Is arterial media hypertrophy in spontaneously hypertensive rats a consequence of or a cause for hypertension? *Clinical Science* 1980; **59 Suppl 6**:331s-333s.http://www.ncbi.nlm.nih.gov/pubmed/7449279AccessedJune 21, 2017.

15. Owens GK, Rabinovitch PS, Schwartz SM. Smooth muscle cell hypertrophy versus hyperplasia in hypertension. *Proceedings of the National Academy of Sciences* 2006; **78**(12):7759–7763. doi:10.1073/pnas.78.12.7759.

16. Olivetti G, Melissari M, Marchetti G, Anversa P. Quantitative structural changes of the rat thoracic aorta in early spontaneous hypertension. Tissue composition, and hypertrophy and hyperplasia of smooth muscle cells. *Circulation Research* 1982; **51**(1):19–26. doi:10.1161/01.RES.51.1.19.

17. Kozerke S, Scheidegger MB, Pedersen EM, Boesiger P. Heart motion adapted cine phase-contrast flow measurements through the aortic valve. *Magnetic Resonance in Medicine* 1999; **42**(5):970–978. doi:10.1002/(SICI)1522-2594(199911)42:5<970::AID-MRM18>3.0.CO;2-I.

18. Emmott A, Garcia J, Chung J, et al. Biomechanics of the Ascending Thoracic Aorta: A Clinical Perspective on Engineering Data. *The Canadian journal of cardiology* 2016; **32**(1):35–47. doi:10.1016/j.cjca.2015.10.015.

19. Beller CJ, Labrosse MR, Thubrikar MJ, Robicsek F. Role of Aortic Root Motion in the Pathogenesis of Aortic Dissection. *Circulation* 2004; **109**(6):763–769. doi:10.1161/01.CIR.0000112569.27151.F7.

20. Beller CJ, Labrosse MR, Thubrikar MJ, Robicsek F. Finite element modeling of the thoracic aorta: including aortic root motion to evaluate the risk of aortic dissection. *Journal of Medical Engineering & Technology* 2009.http://www.tandfonline.com/doi/abs/10.1080/03091900600687672AccessedJanuary 14, 2016.

21. Gasser TC, Holzapfel GA. Modeling the propagation of arterial dissection. *European Journal of Mechanics - A/Solids* 2006; **25**(4):617–633. doi:10.1016/j.euromechsol.2006.05.004.

22. Pasta S, Phillippi JA, Gleason TG, Vorp DA. Effect of aneurysm on the mechanical dissection properties of the human ascending thoracic aorta. *The Journal of Thoracic and Cardiovascular Surgery* 2012; **143**(2):460–467. doi:10.1016/J.JTCVS.2011.07.058.

23. Wang L, Roper SM, Luo XY, Hill NA. Modelling of tear propagation and arrest in fibre-reinforced soft tissue subject to internal pressure. *Journal of Engineering Mathematics* 2015; **95**(1):249–265. doi:10.1007/s10665-014-9757-7.

24. Wang L, Roper SM, Hill NA, Luo X. Propagation of dissection in a residually-stressed artery model. *Biomechanics and Modeling in Mechanobiology* 2017; **16**(1):139–149. doi:10.1007/s10237-016-0806-1.

25. Gültekin O, Hager SP, Dal H, Holzapfel GA. Computational modeling of progressive damage and rupture in fibrous biological tissues: application to aortic dissection. *Biomechanics and Modeling in Mechanobiology* 2019; **18**(6):1607–1628. doi:10.1007/s10237-019-01164-y.

26. Pasta S, Phillippi JA, Gleason TG, Vorp DA. Effect of aneurysm on the mechanical dissection properties of the human ascending thoracic aorta. *The Journal of Thoracic and Cardiovascular Surgery* 2012; **143**(2):460–467. doi:10.1016/j.jtcvs.2011.07.058.

27. Noble C, van der Sluis O, Voncken RMJ, et al. Simulation of arterial dissection by a penetrating external body using cohesive zone modelling. *Journal of the Mechanical Behavior of Biomedical Materials* 2017; **71**(Submitted):95–105. doi:10.1016/j.jmbbm.2017.03.004.

28. Noble C, Smulders N, Lewis R, et al. Controlled peel testing of a model tissue for diseased aorta. *Journal of Biomechanics* 2016; **49**(15):3667–3675. doi:10.1016/j.jbiomech.2016.09.040.

29. Sommer G, Gasser TC, Regitnig P, Auer M, Holzapfel GA. Dissection properties of the human aortic media: an experimental study. *Journal of biomechanical engineering* 2008; **130**(2):021007. doi:10.1115/1.2898733.

30. FitzGibbon B, McGarry P. Development of a novel test method to investigate mode II fracture and dissection of arteries. 2020. doi:10.31224/OSF.IO/D3JBR.

31. Concannon J, Hynes N, McMullan M, et al. Development of an MRI/FEA framework for Analysis of Subject-Specific Aortic Compliance: Part I - Development of a dual-VENC 4D Flow MRI Protocol for Measurement of Heterogeneous non-linear vessel Deformation. doi:10.31224/OSF.IO/SPZGD.

32. M Moerman K. GIBBON: The Geometry and Image-Based Bioengineering add-On. *The Journal of Open Source Software* 2018; **3**(22):506. doi:10.21105/joss.00506.

33. Concannon J, Dockery P, Black A, et al. Quantification of the regional bioarchitecture in the human aorta. *Journal of Anatomy* 2020; **236**(1):142–155. doi:10.1111/joa.13076.

34. Nolan DR, Gower AL, Destrade M, Ogden RW, McGarry JP. A robust anisotropic hyperelastic formulation for the modelling of soft tissue. *Journal of the Mechanical Behavior of Biomedical Materials* 2014; **39**:48–60. doi:10.1016/j.jmbbm.2014.06.016.

35. Fereidoonnezhad B, O'Connor C, McGarry P. A new anisotropic soft tissue model for elimination of unphysical auxetic behaviour. *Journal of Biomechanics* 2020. doi:10.31224/OSF.IO/G6DSE.

36. Nolan DR, McGarry JP. On the Compressibility of Arterial Tissue. *Annals of Biomedical Engineering* 2016; **44**(4):993–1007. doi:10.1007/s10439-015-1417-1.

37. McGarry JP, McHugh PE. Modelling of in vitro chondrocyte detachment. *Journal of the Mechanics and Physics of Solids* 2008; **56**(4):1554–1565. doi:10.1016/j.jmps.2007.08.001.

38. McGarry JP, Ó Máirtín É, Parry G, Beltz GE. Potential-based and non-potential-based cohesive zone formulations under mixed-mode separation and over-closure. Part I: Theoretical analysis. *Journal of the Mechanics and Physics of Solids* 2014; **63**(1):336–362. doi:10.1016/j.jmps.2013.08.020.

39. Heistad DD, Marcus ML, Law EG, Armstrong ML, Ehrhardt JC, Abboud FM. Regulation of blood flow to the aortic media in dogs. *Journal of Clinical Investigation* 1978; **62**(1):133–140. doi:10.1172/JCI109097.

40. Marcus ML. Effects of chronic hypertension on vasa vasorum in the thoracic aorta. *Cardiovascular Research* 1985; **19**(12):777–781. doi:10.1093/cvr/19.12.777.

41. Stefanadis C, Vlachopoulos C, Karayannacos P, et al. Effect of Vasa Vasorum Flow on Structure and Function of the Aorta in Experimental Animals. *Circulation* 1995; **91**(10).

42. Carlson RG, Lillehei CW, Edwards JE. Cystic medial necrosis of the ascending aorta in relation to age and hypertension. *The American Journal of Cardiology* 1970; **25**(4):411–415. doi:10.1016/0002-9149(70)90006-8.

43. Brandt T, Orberk E, Weber R, et al. Pathogenesis of cervical artery dissections: Association with connective tissue abnormalities. *Neurology* 2001; **57**(1):24–30. doi:10.1212/WNL.57.1.24.

44. Ulbricht D, Diederich NJ, Hermanns-Lê T, Metz RJ, Macian F, Piérard GE. Cervical artery dissection: An atypical presentation with Ehlers-Danlos-like collagen pathology? *Neurology* 2004; **63**(9):1708–1710. doi:10.1212/01.WNL.0000142970.09454.30.

45. Lemaire SA, Russell L. Epidemiology of thoracic aortic dissection. *Nature Reviews Cardiology* 2011; **8**(2):103–113.

46. Nakashima Y, Shiokawa Y, Sueishi K. Alterations of elastic architecture in human aortic dissecting aneurysm. *Laboratory investigation; a journal of technical methods and pathology* 1990; **62**(6):751–60.http://www.ncbi.nlm.nih.gov/pubmed/2359259AccessedFebruary 2, 2018.

47. Abraham PA, Perejda AJ, Carnes WH, Uitto J. Marfan syndrome. Demonstration of abnormal elastin in aorta. *Journal of Clinical Investigation* 1982; **70**(6):1245–1252. doi:10.1172/JCI110723.

48. Yuan S-M, Jing H. Cystic medial necrosis: pathological findings and clinical implications. *Revista Brasileira de Cirurgia Cardiovascular* 2011; **26**(1):107–115. doi:10.1590/S0102-76382011000100019.

49. Laurent S, Boutouyrie P. The Structural Factor of Hypertension: Large and Small Artery Alterations. *Circulation Research* 2015; **116**(6):1007–1021.

50. Sokolis DP, Savva GD, Papadodima SA, Kourkoulis SK. Regional distribution of circumferential residual strains in the human aorta according to age and gender. *Journal of the Mechanical Behavior of Biomedical Materials* 2017; **67**:87–100. doi:10.1016/j.jmbbm.2016.12.003.

51. Kozerke S, Scheidegger MB, Pedersen EM, Boesiger P. Heart motion adapted cine phase-contrast flow measurements through the aortic valve. *Magnetic Resonance in Medicine* 1999; **42**(5):970–978. doi:10.1002/(SICI)1522-2594(199911)42:5<970::AID-MRM18>3.0.CO;2-I.

52. Koster MJ, Matteson EL, Warrington KJ. Large-vessel giant cell arteritis: diagnosis, monitoring and management.

Rheumatology 2018; **57**(suppl_2):ii32–ii42. doi:10.1093/rheumatology/kex424.

53. Corbett JJ, Melms A. Giant Cell Arteritis and Polymyalgia Rheumatica. In: *Neurological Disorders: Course and Treatment: Second Edition*, vol 371. NIH Public Access; 2003:475–479.

54. Redheuil A, Yu W-C, Mousseaux E, et al. Age-Related Changes in Aortic Arch Geometry. *Journal of the American College of Cardiology* 2011; **58**(12):1262–1270. doi:10.1016/j.jacc.2011.06.012.

55. Lentini S, Tancredi F, Benedetto F, Gaeta R. Type A aortic dissection involving the carotid arteries: carotid stenting during open aortic arch surgery. *Interactive CardioVascular and Thoracic Surgery* 2008; **8**(1):157–159. doi:10.1510/icvts.2008.186023.

56. Komiyama M, Morikawa T, Nakajima H, Nishikawa M, Yasui T. High Incidence of Arterial Dissection Associated With Left Vertebral Artery of Aortic Origin. *Neurologia medico-chirurgica* 2001; **41**(1):8–12. doi:10.2176/nmc.41.8.

57. Yoshida K, Tobe S. Dissection and rupture of the left subclavian artery presenting as hemothorax in a patient with von Recklinghausen's disease. *Japanese Journal of Thoracic and Cardiovascular Surgery* 2005; **53**(2):117–119. doi:10.1007/s11748-005-0014-x.

58. Tam AS, Sapp MC, Roach MR. The effect of tear depth on the propagation of aortic dissections in isolated porcine thoracic aorta. *Journal of biomechanics* 1998; **31**(7):673–6.http://www.ncbi.nlm.nih.gov/pubmed/9796691AccessedJuly 18, 2019.

59. Matsumoto T, Hayashi K. Stress and strain distribution in hypertensive and normotensive rat aorta considering residual strain. *J Biomech Eng* 1996; **118**(1):62–73. doi:10.1115/1.2795947.

60. Erbel R, Eggebrecht H. Aortic dimensions and the risk of dissection. *Heart (British Cardiac Society)* 2006; **92**(1):137–42. doi:10.1136/hrt.2004.055111.

61. Schindelin J, Rueden CT, Hiner MC, Eliceiri KW. The ImageJ ecosystem: An open platform for biomedical image analysis. *Molecular Reproduction and Development* 2015; **82**(7–8):518–529. doi:10.1002/mrd.22489.

62. Tsamis A, Krawiec JT, Vorp DA. Elastin and collagen fibre microstructure of the human aorta in ageing and disease: a review. *Journal of the Royal Society, Interface / the Royal Society* 2013; **10**(83):20121004. doi:10.1098/rsif.2012.1004.

63. Trimarchi S, Tsai T, Eagle KA, et al. Acute abdominal aortic dissection: Insight from the International Registry of Acute Aortic Dissection (IRAD). *Journal of Vascular Surgery* 2007; **46**(5):913-919.e1. doi:10.1016/J.JVS.2007.07.030.

64. Evans JM, O'Fallon WM, Hunder GG. Increased incidence of aortic aneurysm and dissection in giant cell (temporal) arteritis: A population-based study. *Annals of Internal Medicine* 1995; **122**(7):502–507. doi:10.7326/0003-4819-122-7-199504010-00004.

65. Evangelista A, Isselbacher EM, Bossone E, et al. Insights from the international registry of acute aortic dissection: A 20-year experience of collaborative clinical research. *Circulation* 2018; **137**(17):1846–1860.

66. Puyvelde J Van, … EV-EJ of, 2016 undefined. Aortic wall thickness in patients with ascending aortic aneurysm versus acute aortic dissection. *academic.oup.com*https://academic.oup.com/ejcts/article-abstract/49/3/756/2465260AccessedJuly 27, 2020.

67. Azizzadeh A, Keyhani K, Miller CC, Coogan SM, Safi HJ, Estrera AL. Blunt traumatic aortic injury: Initial experience with endovascular repair. *Journal of Vascular Surgery* 2009; **49**(6):1403–1408. doi:10.1016/j.jvs.2009.02.234.

68. Benjamin MM, Roberts WC. Fatal aortic rupture from nonpenetrating chest trauma. *Proceedings (Baylor University. Medical Center)* 2012; **25**(2):121–3. doi:10.1080/08998280.2012.11928805.

69. M Moerman K. GIBBON: The Geometry and Image-Based Bioengineering add-On. *The Journal of Open Source Software* 2018; **3**(22):506. doi:10.21105/joss.00506.

70. Feerick EM, McGarry JP. Cortical bone failure mechanisms during screw pullout. *Journal of Biomechanics* 2012; **45**(9):1666–1672. doi:10.1016/j.jbiomech.2012.03.023.

71. Feerick EM, Liu XC, McGarry P. Anisotropic mode-dependent damage of cortical bone using the extended finite element method (XFEM). *Journal of the Mechanical Behavior of Biomedical Materials* 2013; **20**:77–89. doi:10.1016/j.jmbbm.2012.12.004.

72. McEvoy E, Deshpande VS, McGarry P. Transient active force generation and stress fibre remodelling in cells under cyclic loading. *Biomechanics and Modeling in Mechanobiology* 2019; **18**(4):921–937. doi:10.1007/s10237-019-01121-9.

73. Reynolds NH, Ronan W, Dowling EP, Owens P, McMeeking RM, McGarry JP. On the role of the actin cytoskeleton and nucleus in the biomechanical response of spread cells. *Biomaterials* 2014; **35**(13):4015–4025. doi:10.1016/j.biomaterials.2014.01.056.